Full length article

Crystallization kinetics in Ge-rich Ge$_x$Te alloys from large scale simulations with a machine-learned interatomic potential

Dario Baratella, Omar Abou El Kheir, Marco Bernasconi *

Department of Materials Science, University of Milano-Bicocca, Via R. Cozzi 55, Milano, I-20125, Italy

ARTICLE INFO

ABSTRACT

A machine-learned interatomic potential for Ge-rich Ge$_x$Te alloys has been developed aiming at uncovering the kinetics of phase separation and crystallization in these materials. The results are of interest for the operation of embedded phase change memories which exploits Ge-enrichment of GeSbTe alloys to raise the crystallization temperature. The potential is generated by fitting a large database of energies and forces computed within Density Functional Theory with the neural network scheme implemented in the DeePMD-kit package. The potential is highly accurate and suitable to describe the structural and dynamical properties of the liquid, amorphous and crystalline phases of the wide range of compositions from pure Ge and stoichiometric GeTe to the Ge-rich Ge$_x$Te alloy. Large scale molecular dynamics simulations have suggested a crystallization mechanism which depends on temperature. At 600 K, segregation of most of Ge in excess was observed to occur on the ns time scale followed by crystallization of nearly stoichiometric GeTe regions. At 500 K, nucleation of crystalline GeTe was observed to occur before phase separation, followed by a slow crystal growth due to the concurrent expulsion of Ge in excess.

1. Introduction

Chalcogenide GeSbTe (GST) phase change alloys are employed in emerging new electronic non-volatile memories called Phase Change Memories (PCMs) [1–4]. These devices feature a rapid and reversible transition of the active material between the crystalline and amorphous phases upon Joule heating. The two phases correspond to the two states of the memory which can be discriminated thanks to a large contrast in the electrical resistivity. Readout of the memory consists of the measurement of the electrical resistance at low bias, while programming is achieved by applying current pulses to amorphize the crystal via melting (reset) or to recrystallize the amorphous phase (set).

PCMs based on the flagship compound Ge$_2$Sb$_2$Te$_5$ (GST225), which is a pseudobinary alloy on the GeTe-Sb$_2$Te$_3$ tie-line, was brought to market in 2017 by Intel and Micron in a 3D cross-bar architecture (3D XPoint™) [5]. More recently, PCMs have also gained attention for embedded applications, in particular for the automotive sector [6,7]. The crystallization temperature T$_x$ of the most commonly used GST225 (420–440 K) [8] is, however, too low for applications in embedded memories that require data retention at higher temperatures. In fact, a compulsory fabrication step of embedded memories is the soldering process in which the device is exposed to 530 K for a few minutes after the microcontroller code was written in the memory [7]. To meet this requirement, various materials alternative to GST225 have

been explored, including InSbTe, GaSbTe, and InGeTe alloys [9–11]. Additionally, doping with *N* or *O* atoms [12] and enrichment with Sb and Ge have been proposed [13]. Among these options, Ge-rich GeSbTe alloys emerged recently as the most promising materials with T$_x$ exceeding 600 K for Ge-rich alloys on the Ge-Sb$_2$Te$_3$ tie-line [14–17]. Several high density embedded memories for microcontrollers have been since then reported in literature [18–21].

The raise in T$_x$ of Ge-rich GST alloys is ascribed to the segregation of Ge atoms and phase separation into pure Ge and Ge-poor GST alloy during the crystallization process [15]. The crystallization is supposed to be slowed down by the mass transport involved in the phase separation, resulting in longer times for crystal nucleation. Evidences of the phase separation were reported in both the set process [15,22–29] and the forming operation of the memory (initialization by the first programming pulse) [16]. However, the inhomogeneity due to phase separation could cause a high cell-to-cell variability. Moreover, a drift in the electrical resistance with time was reported in both the set and reset states. A resistance drift in the reset state (amorphous phase) is common to all phase change materials as it is ascribed to structural relaxations towards a more stable amorphous structure. The resistance drift in the set state (crystalline), instead, is peculiar to Ge-rich GST alloys as it is due to the presence of a residual Ge-rich amorphous

---

* Corresponding author.
  E-mail address: marco.bernasconi@unimib.it (M. Bernasconi).

region close to the bottom electrode in the phase separated system [30]. Gaining a deeper understanding of the segregation and crystallization processes is thus mandatory to mitigate these detrimental effects.

Several details of the overall process are, however, unclear. Although several works have revealed the presence of amorphous Ge and of a cubic crystalline phase of GST [14,22–29], the composition of the cubic phase is unclear because analytical tools such as electron energy loss spectroscopy or energy dispersive X-ray measurements provide only a composition averaged over different grains including pure Ge grains. The presence of crystalline GeTe [24] and of Sb-rich alloys [31,32] was also detected.

In this respect, atomistic simulations can provide useful insights on both the crystallization and segregation processes. Simulations based on Density Functional Theory (DFT), for instance, revealed that the amorphous phase of GST alloys is unstable with respect to Ge segregation for Ge content above 50% [33]. A high throughput DFT study also suggested that off-stoichiometric compositions (off the GeTe-Sb_2Te_3 tieline) might crystallize in a metastable cubic phase at the operation conditions of the memories [34]. These DFT works, however, have only addressed the thermodynamics of the phase transformation and not its kinetics because of the limitations in the time and length scales of DFT simulations.

A route to overcome the limitations of DFT methods is the development of machine-learned interatomic potentials generated by fitting a database of DFT energies and forces. In the past, an interatomic potential for GeTe [35] was generated within the Neural Network (NN) scheme proposed by Behler and Parrinello [36], while more recently interatomic potentials for stoichiometric GST225 [37] were generated with the NN scheme implemented in the DeePMD code [38–40] or with the Gaussian Approximation Potential [41,42].

In the perspective of developing an interatomic potential for large scale simulations of Ge-rich GST alloys, we here address the study of the simpler Ge-rich Ge_xTe binary alloy that shares several properties with the ternary GST system and for which detailed experimental data are available from time resolved reflectivity, X-ray diffraction, transmission electron microscopy and Raman spectroscopy [43–45]. Integration of Ge-rich Ge_xTe alloys in PCMs was also reported in Ref. [46]. We considered in particular the composition Ge_2Te which is close to the $Ge_{63}Te_{37}$ alloy studied experimentally in Ref. [43].

We developed a NN potential suitable to describe Ge_2Te and the products of its crystallization process, stoichiometric GeTe and pure Ge, by using the DeePMD code [38–40] already employed in our recent work on GST225 [37]. We validated the potential by analyzing the structural and dynamical properties of Ge_2Te, GeTe, and Ge in the crystalline, liquid, and amorphous phases. We also considered more Ge-rich Ge_xTe alloys that might form during crystallization. Then, we exploited the potential to perform large-scale simulations of the crystallization and phase separation processes.

2. Methods

We generated the NN potential for Ge-rich Ge_xTe alloys by fitting a database of DFT energies, forces, and virial tensors within the framework implemented in the DeePMD code [38–40]. The database consists of 115000 atomic configurations of Ge, GeTe and Ge_2Te in the amorphous, liquid and crystalline phases, supplemented by 5000 configurations of the more Ge-rich amorphous alloys Ge_9Te and Ge_3Te, and of the interface between amorphous Ge (a-Ge) and amorphous GeTe (a-GeTe) that might form during the crystallization process. Amorphous and liquid Ge, GeTe and Ge_2Te were modeled in cells of 144, 108 and 100 atoms (composition $Ge_{67}Te_{33}$), respectively. Amorphous Ge_9Te, Ge_3Te and the a-Ge/a-GeTe interface were modeled in cells of 300 atoms. The crystalline phases of Ge and GeTe were modeled in cells with 64 and 96 atoms. The atomic configurations were extracted from DFT molecular dynamics (MD) simulations by using the CP2k code [47]. The Perdew–Burke–Ernzherof (PBE) exchange

Table 1
Number of configurations included in the database for each composition and phase; l & a stands for liquid and amorphous phases; a-Ge/a-GeTe interface stands for the interface between amorphous Ge and amorphous GeTe.

Phase	Number of configurations
Ge l & a	27 000
GeTe l & a	35 000
Ge_2Te l & a	46 000
Crystalline Ge	3400
Crystalline GeTe	3600
Ge_9Te l & a	1000
Ge_3Te l & a	2000
a-Ge/a-GeTe interface	2000

and correlation functional [48] and Goedecker–Teter–Hutter (GTH) norm conserving pseudopotentials with s and p valence electrons were used [49,50]. Kohn–Sham orbitals were expanded in a Triple-Zeta-Valence-plus-Polarization (TZVP) basis set while the electronic density was expanded in plane waves up to a kinetic cutoff of 100 Ry. The Brillouin Zone (BZ) integration was restricted to the Γ-point in all MD simulations. The time step was set to 2 fs and configurations were extracted every 100–200 fs. The number of configurations for each phase and composition is given in Table 1. We recalculated energies, forces, and stresses for each configuration added to the database with a higher accuracy by increasing the kinetic energy cutoff for the plane-waves expansion of the electronic density to 400 Ry and by using a $4 \times 4 \times 4$ k-point mesh for the BZ integration. A Fermi–Dirac smearing in the occupation of Kohn–Sham states was used with an electronic temperature of 300 K. The RMSE in the forces by using the Γ-point only with respect to the $4 \times 4 \times 4$ mesh is 85 meV/Å for the amorphous phase and 110 meV/Å in the liquid phase of Ge2Te. This error is irrelevant for the generation of the trajectories to sample the phase space, but the higher accuracy of the finer mesh is mandatory for the fitting of the NN potential.

In NN schemes for the generation of interatomic potentials, the total energy of the system is written as the sum of individual atomic energies that depend on the local environment of each atom [36]. In the DeePMD scheme the local environment is encoded by local descriptors which are generated by an embedded neural network. A second neural network (fitting network) is built for the calculation of energies and forces with the local descriptors as input layer. We designed the embedded network with three hidden layers of 40, 80, and 160 nodes. All nodes are fully connected with those in the precedent and following layers. The cutoff radius r_c was set to 7 Å, which is beyond the third coordination shell of our systems, while the smoothing radius r_s was set to 2 Å in the implementation of Ref. [39]. The maximum number of neighbors was set to 80. We also exploited the attention mechanism that was recently implemented in the DeePMD code [39]. This method, initially formulated in the context of natural language processing, has emerged as a powerful tool in several applications of deep learning [51]. In DeePMD, the attention method is exploited for building trainable descriptors in the embedded network that allow for a faster learning [39]. Due to the heterogeneity of the training database, the attention method was particularly useful to speed up the learning process for our systems and to reduce overfitting. Details on the implementation of the attention method are given in Ref. [39]. Roughly speaking, with the attention mechanism the descriptor of each atom is defined not only by its environment but also by the environment of its neighbors. Finally, the network for the fitting of energy and forces consists of 3 hidden layers with 320 nodes each. In the embedding and fitting network, we have used the hyperbolic tangent as an activation function.

The NN potential was generated in an iterative manner. A first version of the potential was generated by using a small training database of about 6000 configurations of Ge, GeTe and Ge_2Te. Then, the potential is used to perform MD simulations that provide high-energy

configurations to enrich the training database for a second generation of the potential and at the same time we enriched the database with additional atomic configurations extracted from DFT-MD simulations at different densities and exploring a wider temperature range.

We iterated the procedure until the error on forces and energies did not improve any more nor the validation on the structural properties of the liquid, amorphous and crystalline phases improved further with respect to the very good results that we will illustrate in Section 3.1. We generated a first version of the potential in which only configurations with Ge, GeTe or Ge_2Te stoichiometry were included in the training database (see Table 1). Then we generated a second version of the potential by including in the training database also the configurations for the other more Ge-rich compositions, Ge_9Te and Ge_3Te, and for the a-Ge/a-GeTe interface (see Table 1).

Structural and dynamical properties obtained from NN simulations were compared with results from DFT-MD simulations performed with the CP2k code with the same parameters given above. NN-MD simulations were performed by using the LAMMPS code [52] as MD driver with the DeePMD plugin.

To assess whether an atom is crystalline in the simulations of the crystallization process, we used the Steinhardt order parameters Q_n^{dot} [53,54]. In general, the Q_n^{dot} parameter of order n is defined for each atom i by

$$Q_n^{dot} = \frac{1}{N_i} \sqrt{\sum_{j=1}^{N_i} \sum_{m=-n}^{n} q_{nm,i} q_{nm,j}^*} \tag{1}$$

$$q_{nm,i} = \frac{1}{N_i} \sum_{j=1}^{N_i} Y_{nm} \left(\hat{\mathbf{r}}_{ij} \right), \tag{2}$$

where N_i in the number of neighbors of atom i up to a given cutoff, j is the neighbors index, Y_{nm} is the n order spherical harmonic with degree m, and $\hat{\mathbf{r}}_{ij}$ is the unit vector connecting the two atoms. For the crystallization of GeTe, we considered the Q_4^{dot} order parameter, but also the Q_6^{dot} has been considered for some analysis, as it will be discussed in the relevant section. The distribution of Q_4^{dot} and Q_6^{dot} in crystalline and amorphous phases of GeTe is shown in Fig. S1 in the Supplementary Material. A threshold of $Q_4^{dot} = 0.87$ was chosen for an atom to be crystalline.

To assess whether a Ge atom is segregated in regions of a-Ge, we calculated the SOAP (Smooth Overlap of Atomic Position) similarity kernel k_j for each atom [55]. k_j quantifies the similarity of the atomic environment around atom j with a reference atomic environment which is taken here as the average environment in a-Ge at 600 K. k_j is a number that ranges from 0, when the atomic environment is totally different from that of the reference system, to 1 when it is identical. In the SOAP formalism the local atomic density around each atom j is expressed as a sum of Gaussian functions (here with broadening $\sigma_{at} = 0.3$ Å) centered on the position of its neighbors up to a given cutoff (here 9 Å). Then the density around atom j is expanded in spherical harmonics and radial basis functions $g_b(|\mathbf{r}|)$ as $\rho_j(\mathbf{r}) = \sum_{blm} c_{blm} g_b(|\mathbf{r}|) Y_{lm}(\hat{\mathbf{r}})$. The coefficients of this expansion define the so-called power spectrum matrix $p(j)_{b_1 b_2 l} = \pi \sqrt{8/(2l+1)} \sum_m (c_{b_1 lm})^* c_{b_2 lm}$ whose elements are turned into a vector $\mathbf{p}_j$ from which the SOAP kernel k_j is calculated as $k_j = (\mathbf{p}_j/|\mathbf{p}_j| \cdot \mathbf{p}_{ref}/|\mathbf{p}_{ref}|)^\xi$, where $\mathbf{p}_{ref}$ is the average power spectrum of the atoms in the atomic environment of the reference system and ξ is an integer set to 2 in our case. The SOAP similarity kernel has been used in a variety of studies to analyze the atomic structure [56,57] and very recently to discriminate between the crystalline and amorphous/liquid phases in GST alloys [58]. In this work, we calculated the SOAP kernel using the DScribe Python package [59,60] and the ASE Python library [61]. For the purpose of identifying the a-Ge regions only, this approach is computationally more efficient than using the embedded NN for the structural descriptors themselves. In the simulation of the crystallization of $Ge_1Sb_2Te_4$ [58], which is structurally similar in the amorphous and cubic crystalline phase to GeTe, it was shown that the SOAP and the Q_4^{dot} parameter produce very similar results. Here, we have used Q_4^{dot} to identify crystalline atoms for the sake of comparison with previous works on the crystallization of GeTe [62].

3. Results and discussion

3.1. Validation of the neural network potential

The accuracy of the NN potential is assessed by the cumulative distribution of the error on energies, forces and virial tensors shown in Fig. 1 for Ge_2Te, GeTe and Ge. GeTe has the largest errors, while Ge_2Te and Ge have significantly lower errors. Overall, the root mean square error (RMSE) on the energy is 4.6 meV/atom, on forces is 103 meV/Å and on virial is 12.8 meV/atom on the whole training database including the configurations for Ge_9Te, Ge_3Te and the a-Ge/a-GeTe interface. We remark that the typical average error obtained with DeePMD for highly disordered phases of multicomponent systems like ours (i.e liquid and/or amorphous phases) are in the range 2–7 meV/atom and 90–145 meV/Å [63–66]. In Section 2, we mentioned that we generated a first version of the potential by including in the training database only configurations for Ge, GeTe and Ge_2Te. For this potential, the RMSE on the energies and forces was 4.4 meV/atom and 105 meV/Å, but on the test database of the Ge_9Te, Ge_3Te and the a-Ge/a-GeTe interface configurations, the RMSE was sizeably larger, i.e. 12.9 meV/atom and 112 meV/Å. The final potential, trained also on the configurations of Ge_9Te, Ge_3Te and of the a-Ge/a-GeTe interface, features a RMSE for this latter part of the training database of 6.3 meV/atom and 117 meV/Å.

The NN potential has then been validated on the properties of the liquid, amorphous and crystalline phases as described in the separate sections below for pure Ge, stoichiometric GeTe and Ge_2Te. In Section 3.1.2, we also discuss the validation of the potential on the structural properties of the amorphous phase with Ge_9Te and Ge_3Te compositions which might appear during the process of phase separation and crystallization of Ge_2Te.

3.1.1. The liquid phase

We computed the structural properties of liquid Ge at 1250 K from NN-MD simulations in a 2400-atom model and from DFT-MD simulations in a 300-atom model. In the perspective to study later the amorphous phase, we used for the liquid the experimental density of the amorphous phase of 0.0438 atom/Å³ [67]. The models were equilibrated first at 2000 K for 10 ps and then at 1250 K for 20 ps. The structural properties were evaluated from the last 10 ps of the NVT run at 1250 K. The pair correlation function, the distribution of the coordination numbers and the bond angle distribution function of liquid Ge from NN and DFT simulations are compared in Fig. 2.

The structural properties of liquid GeTe (4096-atom model) and of liquid Ge_2Te (2400-atom model) from NN-MD simulations were compared with DFT-MD results for 300-atom models for both compositions. For GeTe, we used the experimental equilibrium density of the liquid phase at 1150 K of 0.03294 atom/Å³ [68]. Since no experimental data are available for the density of liquid Ge_2Te, and in the perspective to study the amorphous phase, we generated an amorphous model within DFT-MD by quenching from 1200 K to 300 K in 100 ps in the NPT ensemble which yielded an equilibrium density at 300 K of 0.0355 atom/Å³. To this aim, we used the Grimme (D3) semiempirical potential [69] for van der Waals (vdW) interactions which is needed to avoid the coalescence of nanovoids in the liquid phase as discussed in Ref. [70]. Liquid Ge_2Te was then simulated without vdW corrections at the same density of the amorphous phase of 0.0355 atoms/Å³. In fact, all the results reported in the following still refer to simulations without vdW interactions as we want to validate the NN potential over DFT-PBE data. vdW interactions might be later added in simulations with the NN potential even by using different schemes.

The liquid models were equilibrated first at 2000 K for 10 ps and then for 20 ps at 1150 K for GeTe and at 1200 K for Ge_2Te, which are well above the melting temperature (990 K for the melting of GeTe [71] and for the incongruent melting of Ge_2Te, the liquidus temperature of Ge_2Te is instead 1150 K [72]). Structural properties were calculated in
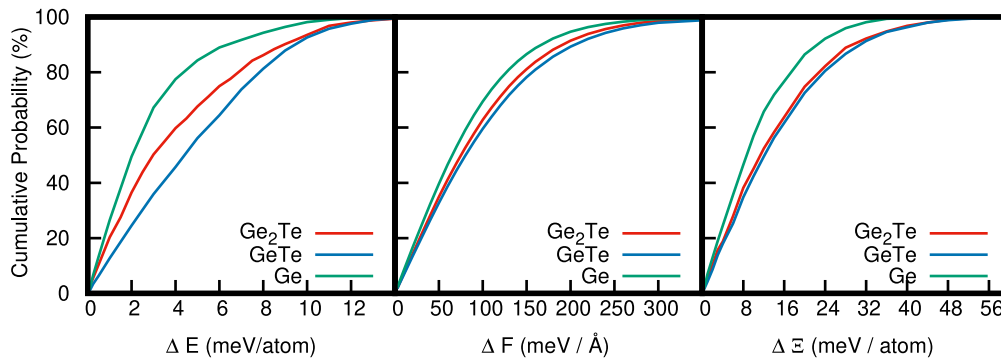
Fig. 1. Cumulative fraction of error on energies, forces and virial of the NN potential in Ge, GeTe and Ge$_2$Te.
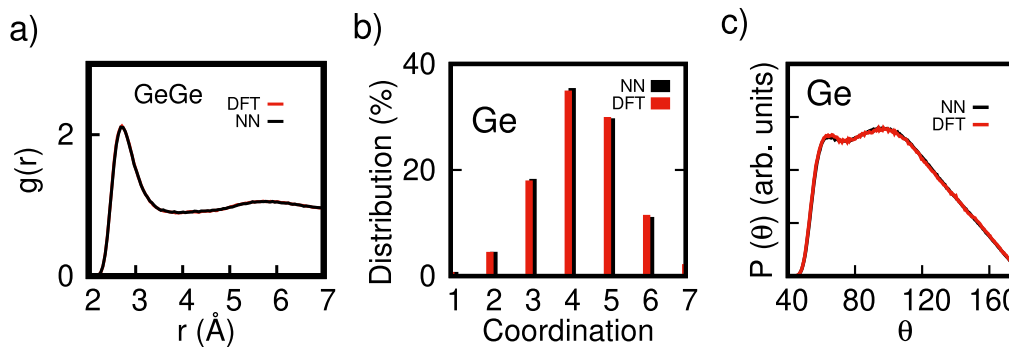

Fig. 2. Structural properties of liquid Ge at 1250 K from NN-MD (black lines, 2400 atoms) and DFT-MD (red lines, 300 atoms). The experimental density of the amorphous phase of 0.0438 atom/Å^3 is used. (a) Pair correlation function. (b) Distribution of the coordination numbers by assuming a bonding cutoff of 3 Å. Ge is primarily 4-fold and 5-fold coordinated, with a minority of 3-fold and 6-fold coordinated atoms. The average coordination number of Ge is 4.29 with the NN potential and 4.31 with DFT. (c) Bond angle distribution function. The peak around 100° is a feature of the Ge atoms in a tetrahedral environment, while the peak at 60° highlights overcoordinated 5-fold and 6-fold atoms. (For interpretation of the references to color in this figure legend, the reader is referred to the web version of this article.)

Table 2
Average partial coordination numbers in liquid Ge$_2$Te at 1200 K and liquid GeTe at 1150 K. DFT data are reported in parenthesis.

		Ge	Te	Total
Ge$_2$Te	Ge	2.53 (2.53)	1.50 (1.51)	4.04 (4.04)
	Te	3.07 (3.07)	0.07 (0.07)	3.14 (3.14)
GeTe	Ge	1.26 (1.31)	2.73 (2.63)	3.99 (3.94)
	Te	2.73 (2.63)	0.17 (0.19)	2.90 (2.82)

Table 3
Diffusion coefficients in liquid Ge$_2$Te at 1100 K and liquid GeTe at 1120 K from NN and DFT (in parenthesis) simulations, all with a 300-atom cell.

		D (10^{-5} cm^2/s)	
		Ge	Te
Ge$_2$Te	1100 K	9.1 (8.7)	5.5 (5.9)
GeTe	1120 K	6.6 (6.3)	4.5 (5.0)

the last 10 ps. The pair correlation functions, the distribution of the coordination numbers and the bond angle distribution of liquid Ge$_2$Te and GeTe from NN and DFT simulations are compared in Fig. 3. The bonding cutoff of 3 Å for Ge-Ge, 3.22 Å for Ge-Te and 3 Å for Te-Te have been used. The average partial coordination numbers are shown in Table 2.

Overall, the NN potential reproduces very well the structural properties of the liquid phase for all the three compositions, i.e. pure Ge, GeTe and Ge$_2$Te.

Regarding the dynamical properties, we computed the diffusion coefficient (D) in liquid GeTe and Ge$_2$Te from the mean square displacement (MSD) and the Einstein relation $MSD = 6Dt$ in 30 ps simulations. Data from NN and DFT simulations with the same 300-atom cell are compared in Table 3 at 1100 K for Ge$_2$Te and at 1120 K at GeTe. These two temperatures were chosen because of the availability of DFT-NVE simulations generated for other purposes.

Both in Ge$_2$Te and GeTe, the NN potential slightly overestimates the diffusion coefficients by less than 10%. For the NN potential, we also computed D for different size L of the cubic cell as shown in Fig. 4a to extract the viscosity η from the scaling law [73]

$$D(L) = D_\infty - \frac{2.387 k_B T}{6\pi\eta L}, \tag{3}$$

The linear fitting yields $D_\infty = 6.5$ cm^2/s and $\eta = 0.98$ mPa·s for GeTe at 1120 K and $D_\infty = 9.1$ cm^2/s and $\eta = 0.75$ mPa·s for Ge$_2$Te at 1100 K. The resulting value of η for GeTe is similar to previous results from NN simulations of Ref. [70].

The diffusion coefficient (total and resolved per species) has then been computed on a wide temperature range in the liquid and supercooled liquid phases from NN simulations 800 ps long at each temperature with a large 4096-atom cell, as shown in Fig. 4. The diffusion coefficient of Ge$_2$Te is fitted by a Cohen–Grest function [74] $\log(D(T)) = A - 2B/(T - T_0 + [(T - T_0)^2 + 4CT]^{1/2})$ which is suitable for the supercooled phase of fragile liquids. According to Angell [75], a supercooled liquid is classified as fragile if the viscosity η remains very low down to temperatures close to the glass transition temperature T$_g$, where a steep, super-Arrhenius behavior is observed up to the high value of η expected at T$_g$. A similar super-Arrhenius behavior is expected for the diffusion coefficient D given its inverse proportionality with the viscosity η according to the Stokes–Einstein relation. On the contrary, the viscosity of an ideal strong liquid follows an Arrhenius behavior from the melting down to T$_g$. The fitting parameters for Ge$_2$Te amount to $A = -3.59$ (-3.54), $B = 337$ K (324 K), $C = 10.5$ K (12.03 K) and $T_0 = 410$ K (425 K) with the values in parenthesis referring
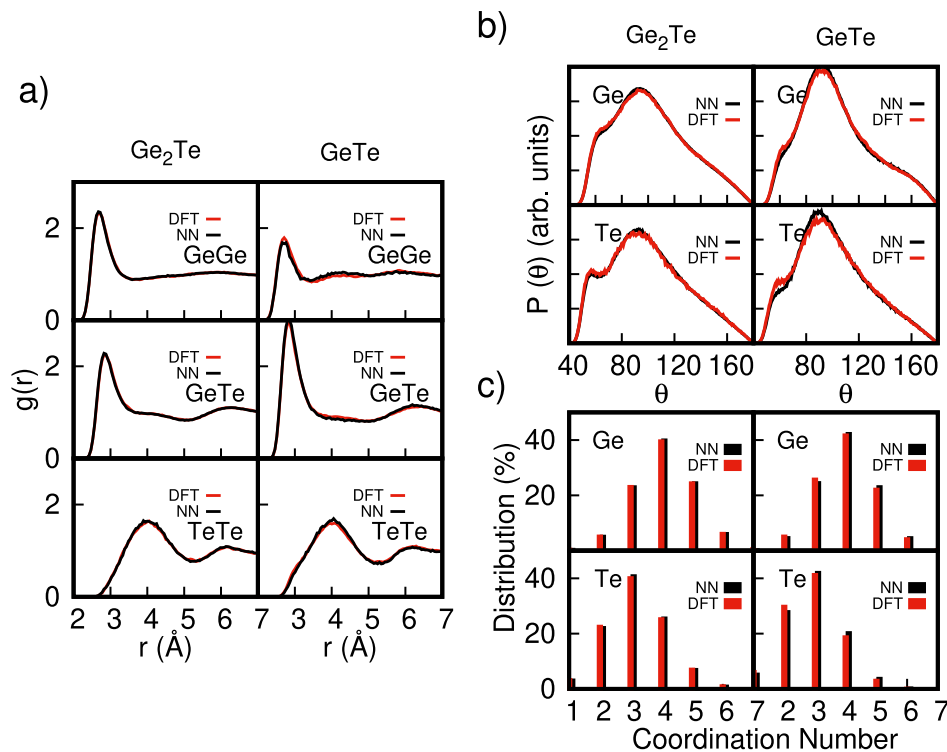
Fig. 3. Structural properties of liquid Ge$_2$Te at 1200 K (left panels) and liquid GeTe at 1150 K (right panels) from DFT and NN simulations. (a) Partial pair correlation functions. (b) Bond angle distribution. (c) Distribution of coordination numbers.

to the diffusion coefficient of Ge atoms only. For GeTe, the diffusion coefficient follows an Arrhenius behavior $D = D_0 e^{-E_a/(k_B T)}$ down to 500 K as shown in Fig. 4 and in agreement with previous NN results in Ref. [70], due to the breakdown of the Stokes-Einstein relation at low temperatures. The fitting parameters for GeTe are $E_a = 0.32$ eV and $D_0 = 1.77 \cdot 10^{-3}$ cm^2/s. The super-Arrhenius behavior in D for GeTe would appear at lower temperatures, below 500 K, considering that T_g is expected to be higher for Ge$_2$Te than for GeTe. The reported glass transition temperature for pure germanium of about 750 K [76] is indeed higher than the value of 423 K reported for GeTe [77]. For the sake of comparison the diffusion coefficient of pure Ge as a function of temperature is given in Fig. S2 in the Supplementary Material.

3.1.2. The amorphous phase

An amorphous model of Ge was generated by cooling the liquid model from 1250 K to 300 K in 140 ps in both the DFT and NN simulations at the experimental density of a-Ge of 0.0438 atoms/Å^3 [67]. Structural properties were averaged over the last 10 ps of an equilibration run at 300 K lasting 20 ps. NN and DFT results for the pair correlation function, the distribution of the coordination numbers and the bond angle distribution function are compared in Fig. 5.

Amorphous models of Ge$_2$Te (a-Ge$_2$Te) and GeTe (a-GeTe) were obtained by quenching the liquid to 300 K in 100 ps starting from 1200 K for Ge$_2$Te and from 1150 K for GeTe in both NN and DFT simulations. The pair correlation functions, the distribution of the coordination numbers, and the bond angle distribution functions are compared in Fig. 6, while the average partial coordination numbers are given in Table 4. The bonding cutoffs are the same used for the liquid as given above.

The agreement between the NN and DFT results is overall very good for Ge, GeTe and Ge$_2$Te. We just note a slight misfit in the number of 2-fold Te atoms in a-Ge$_2$Te and in the position and intensity of the peak of the Ge-Ge correlation function in a-GeTe, possibly due in part to the variability from model to model in small 300-atom cells as discussed in a previous work on stoichiometric GeTe [35].

Table 4

Average partial coordination numbers in amorphous Ge$_2$Te and GeTe at 300 K from NN and DFT (in parenthesis) simulations.

		Ge	Te	Total
Ge$_2$Te	Ge	2.58 (2.58)	1.53 (1.46)	4.11 (4.04)
	Te	3.11 (2.96)	0.00 (0.00)	3.11 (2.96)
GeTe	Ge	0.83 (0.87)	3.31 (3.18)	4.14 (4.04)
	Te	3.31 (3.18)	0.00 (0.04)	3.31 (3.21)

Turning now to a comparison of the structural properties of Ge$_2$Te and GeTe, we notice that by increasing the fraction of Ge from GeTe to Ge$_2$Te, the fraction of Ge-Ge bonds that favor a tetrahedral environment of Ge [78] also increases. This feature shows up as an increased fraction of 4-fold coordinated Ge in the distribution of the coordination numbers (see Fig. 6) and in the shift to higher angles of the peak in the bond angle distribution. In general, we expect a coexistence of tetrahedral, pyramidal (3-fold coordinated) and defective octahedral coordination (octahedral angles but coordination lower than six) for Ge atoms. The fraction of Ge atoms in tetrahedral configurations can be quantified by using the q-parameter for tetrahedricity introduced in Ref. [79] and defined by $q_j = 1 - \frac{3}{8} \Sigma_{i<k} (\frac{1}{3} + cos(\theta_{ijk}))^2$, where the sum runs over the pairs of atoms bonded to a central atom j and forming a bonding angle θ_{ijk}. The order parameter evaluates to q=1 for the ideal tetrahedral geometry, to q=0 for the 6-fold coordinated octahedral site, to q=5/8 for a 4-fold coordinated defective octahedral site, and q=7/8 for a pyramidal geometry. The distribution of the q-parameter for 4-coordinated Ge atoms is shown in Fig. 6d for amorphous Ge$_2$Te, GeTe and Ge at 300 K. The q-parameter features two peaks in a-GeTe due to the coexistence of tetrahedral and defective octahedral configurations [80]. As discussed in Ref. [81], the integration of the q-parameter in the range 0.8–1.0 gives a good measure of the fraction of tetrahedral Ge which is 24% in GeTe, similar to previous DFT works [80,82]. On the other hand, a-Ge$_2$Te features a single peak centered at the position corresponding to the tetrahedral configuration (as in a-Ge). The peak is, however, very
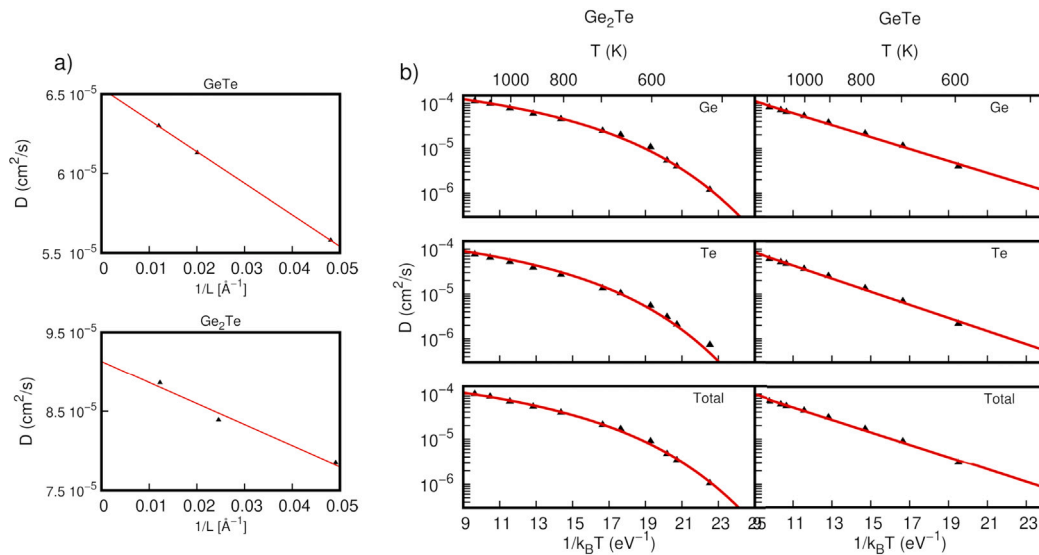
Fig. 4. (a) Linear fitting of the diffusion coefficient (D) with the size L of the cubic supercell for Ge_2Te at 1100 K and GeTe at 1120 K. (b) D as a function of temperature from NN simulations of GeTe and Ge_2Te for (upper panels) Ge atoms only, (central panels) Te atoms only and (bottom panels) the total values averaged over all atoms. The continuous lines are Cohen–Grest (see text) of the data for Ge_2Te and a simple Arrhenius fit for GeTe.
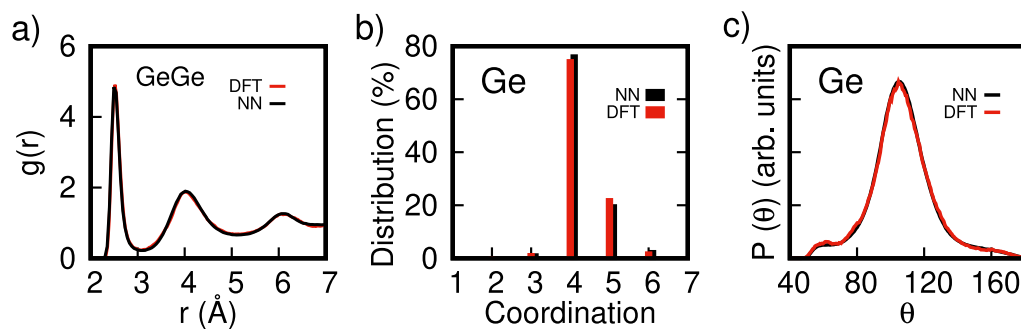

Fig. 5. Structural properties of amorphous Ge at 300 K from NN and DFT simulations. (a) Pair correlation function. (b) Distribution of coordination numbers by assuming a bond cutoff of 3 Å. (c) Bond angle distribution function.
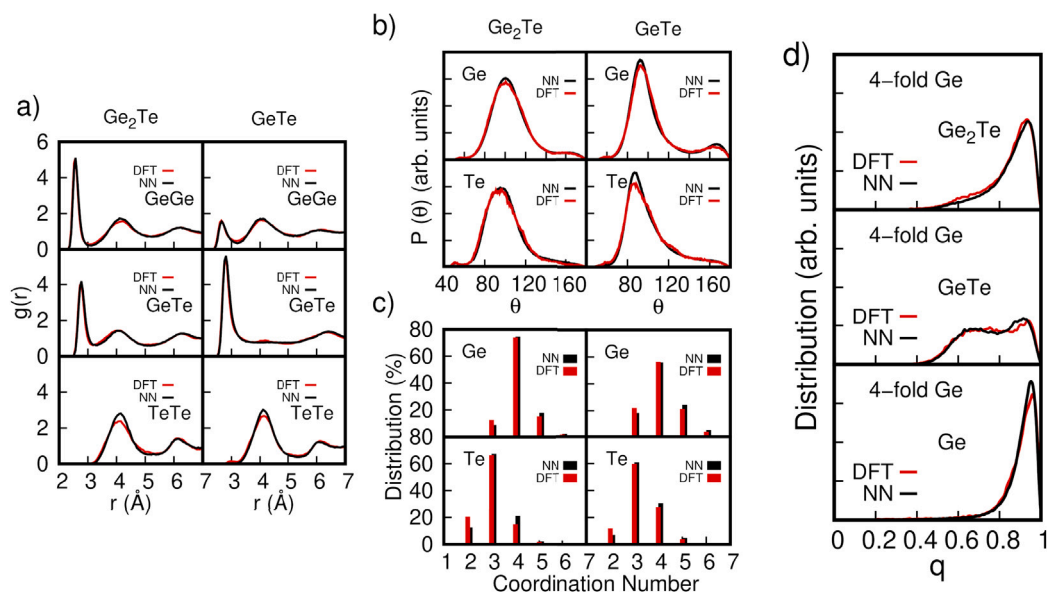

Fig. 6. Structural properties of amorphous Ge_2Te (left panels) and GeTe (right panels) at 300 K from DFT and NN simulations. (a) Partial pair distribution functions. (b) Bond angle distribution functions. (c) Distribution of the coordination numbers. (d) Distribution of the q order parameter for tetrahedricity, also for pure Ge.
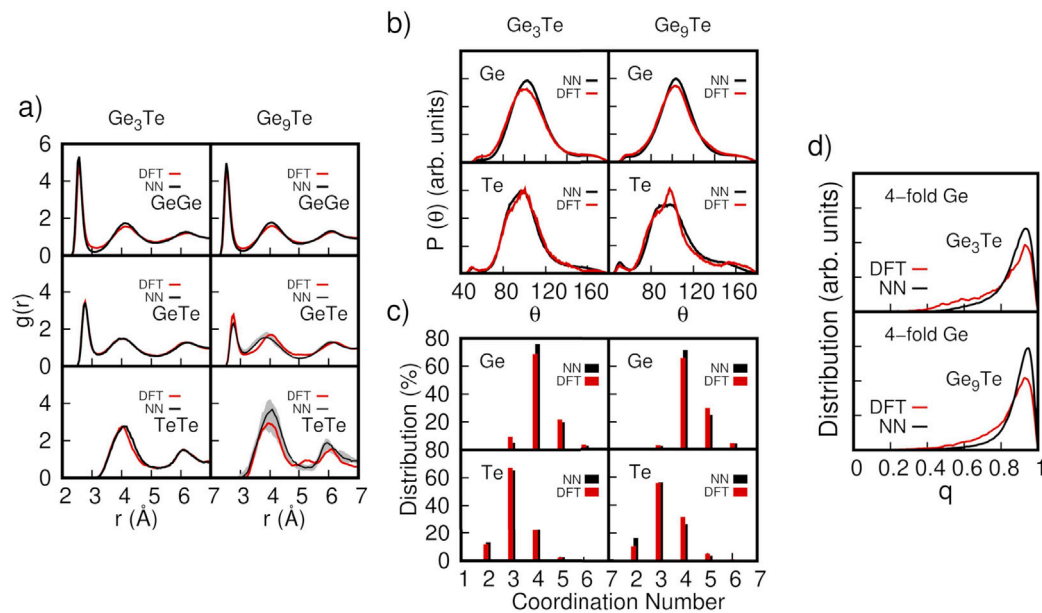
Fig. 7. Structural properties of amorphous Ge_3Te (left panels) and Ge_9Te (right panels) at 300 K from DFT and NN simulations. (a) Partial pair distribution functions. (b) Bond angle distribution functions. (c) Distribution of the coordination numbers. (d) Distribution of the q order parameter for tetrahedricity. The DFT models (red lines) contain 300 atoms while the NN models (black lines) contain 2400 atoms. The gray regions in the pair correlation functions of Ge_9Te indicate the spread in the NN results from seven independent 300-atom models. The misfit between the DFT and NN results for Ge_9Te is due to finite size effects which are particularly relevant for a small content of Te. (For interpretation of the references to color in this figure legend, the reader is referred to the web version of this article.)

broad which suggests that also in Ge_2Te a percentage of Ge atoms are in defective octahedral configurations. By integrating the q-distribution for values greater than 0.8, one obtains a percentage of tetrahedral Ge of approximately 52% in a-Ge_2Te, which is in between the values of 24% and 68% for a-GeTe and a-Ge. Analogously to the liquid phase, the agreement between the NN and DFT results for the amorphous phase is overall very good for Ge, GeTe and Ge_2Te.

We have also assessed the reliability of the NN potential in reproducing the DFT phonon density of states for GeTe and Ge_2Te as shown in Fig. S3 in the Supplementary Material. Finally, we have further assessed the transferability of the NN potential to the more Ge-rich compositions Ge_9Te and Ge_3Te alloys which might appear during the process of phase separation and crystallization of Ge_2Te. Pair correlation functions, bond angles distribution functions and distribution of the coordination numbers for amorphous Ge_9Te (300 atoms at density of 0.042 atoms/$Å^3$) and Ge_3Te (300 atoms at density of 0.03765 atoms/$Å^3$) are compared with DFT results in Fig. 7. The theoretical equilibrium density has been obtained from DFT-NPT simulations as described previously for Ge_2Te.

3.1.3. The crystalline phase

We calculated the energy of crystalline cubic Ge and of trigonal (α-phase) GeTe at different volumes and we fitted the energy as a function of volume by using the Birch–Murnaghan equation of state as shown in Fig. S4 in the Supplementary Material. The resulting fitting parameters from NN and DFT calculations are compared in Table 5 while the equilibrium structural parameters of α-GeTe (space group $R3m$) [83] are given in Table 6. Crystalline α-GeTe, with two atoms per unit cell, can be viewed as a distorted rocksalt geometry with an elongation of the cube diagonal along the [111] direction and an off-center displacement of the inner Ge atom along the [111] direction giving rise to a 3+3 coordination of Ge with three short and stronger bonds and three long and weaker bonds (Peierls distortion, see Table 6). In the conventional hexagonal unit cell of the trigonal phase, the structure can be also seen as an arrangement of GeTe bilayers along the c direction with shorter intrabilayer bonds and longer interbilayers bonds. We mention that the trigonal ferroelectric phase transforms into

Table 5
Fitting parameters of the Birch–Murnaghan equation of state of cubic Ge and trigonal GeTe. V_0 is the equilibrium volume, E_0 the equilibrium energy, B_0 the bulk modulus and B′ its derivative respect to pressure. See Fig. S4 in the Supplementary Material.

	cubic Ge			
Method	E_0 (eV/atom)	V_0 ($Å^3$/atom)	B (GPa)	B′
NN	−106.972	24.22	57.80	4.74
DFT	−106.972	24.22	57.58	4.64
	α-GeTe			
Method	E_0 (eV/atom)	V_0 ($Å^3$/atom)	B (GPa)	B′
NN	−164.671	28.31	29.24	8.58
DFT	−164.671	28.34	28.88	8.55

Table 6
Equilibrium structural parameters of the α-phase of GeTe in the rhombohedral setting from NN and DFT calculations. a is the lattice parameter, α is the angle of the trigonal cell, V is the unit cell volume (two atoms), x assigns the position of Ge atom at (x, x, x) and Te atom at $(-x, -x, -x)$ in crystallographic units. d_{short} and d_{long} are the lengths of the short and long Ge-Te bonds.

Method	a (Å)	α	V ($Å^3$)	x	d_{short} (Å)	d_{long} (Å)
NN	4.416	56.95 °	56.62	0.2344	2.86	3.27
DFT	4.39	57.65 °	56.70	0.2345	2.86	3.26

the cubic paraelectric phase (β-phase, space group $Fm\bar{3}m$) above the Curie temperature of 705 K [84]. In the cubic phase, the alternation of long and short bonds survives in a disordered manner along all equivalent <111> directions as revealed by extended X-ray absorption fine structure (EXAFS), X-ray total diffraction measurements [85,86] and MD simulations [87]. However, more recent molecular dynamics simulations [88] suggest that the order–disorder character of the phase transition is weaker than as inferred from EXAFS data. The β-phase is the structure a-GeTe crystallizes into at the operation conditions of the memory devices.

In summary, the RMSE for the energies and forces (4.6 meV/atom and 103 meV/Å) are similar to other NN potentials in literature for disordered multi-component materials, and the validation of the potential over the properties of liquid, amorphous and crystalline phases is

Table 7
Synoptic table of the simulations at different compositions/conditions.

Name	Atoms	System	T (K)	time (ns)	Starting Conf.
S1	32768	GeTe	600	2	liquid at 1150 K
S2	32768		500	2	liquid at 1150 K
S3	30000	Ge_2Te	600	25	liquid at 1200 K
S4	30000		500	10	liquid at 1200 K
S5	30000		600	12	amorphous at 300 K
S6	30000		500	10	amorphous at 300 K
S7	30000		1200	0.8	end of S3 equilibrated at 300 K
S8	19200	$Ge_{54}Te_{46}$	600	10	liquid at 1200 K

excellent. We remark that the first NN potential that we generated by including in the training database only configurations of Ge, GeTe and Ge_2Te (see Sections 2 and 3.1) reproduces equally well the structural and dynamical properties of all the phases and compositions discussed so far, including those of the more Ge-rich compositions, Ge_9Te and Ge_3Te. As mentioned in Section 3.1, this first potential has, however, a larger RMSE on energies for the more Ge-rich alloys and for the a-Ge/a-GeTe interface configurations. Overall, we judge that our potential is sufficiently accurate to address the study of the crystallization process as discussed in the next section.

3.2. Simulation of the crystallization process

We exploited the NN potential discussed above to perform simulations of the crystallization process in both GeTe and Ge_2Te. We first simulated stoichiometric GeTe to compare the results with previous NN simulations in Ref. [62].

3.2.1. GeTe

We generated a 32768-atom model of a-GeTe at the experimental amorphous density of 0.0333 atom/$Å^3$ [89]. The model was equilibrated first at 2000 K for 10 ps and at 1150 K for 40 ps, and it was then cooled to either 600 or 500 K in 60 ps. Finally, we performed a NVT simulation at the two target temperatures. We name these simulations S1 (600 K) and S2 (500 K) in the synoptic Table 7 which summarize all the simulations we performed at different compositions/conditions. The number of crystalline atoms as a function of time at 600 and 500 K are shown in Fig. 8a. Some small crystalline nuclei of cubic GeTe form and begin to grow after the first 100 ps, as shown in the snapshot of Fig. 8b from the simulation at 600 K. The nucleation time is therefore similar to that obtained in previous NN simulations in Ref. [62] where the first overcritical nucleus appeared after a few hundreds ps in a cell (4096 atom) eight times smaller than ours. We calculated the crystal growth velocity $v_g = dR/dt$, where R is the radius of the crystalline nucleus given in turn by $R(t) = (3N(t)/4\pi\rho)^{\frac{1}{3}}$, where N is the number of atoms in the nucleus and ρ is the density of the crystalline phase (0.0351 atoms/$Å^3$). This assumption is valid only in the early stage of crystallization when the nuclei do not interact with each other or with their periodic image. As an example, the evolution of $R(t)$ as a function of time is shown Fig. S5 in the Supplementary Material for a single crystalline nucleus in GeTe. We computed v_g by averaging over four crystalline nuclei at both temperatures. The resulting v_g reported in Table 8 are slightly higher than those computed in the previous NN simulations of Ref. [62] which yielded 3.6 m/s at 600 K and 0.5 m/s at 500 K. Overall our potential reproduces the crystallization kinetics in a manner very similar to the NN potential of Ref. [62] which was previously used to address several other details of the crystallization process [62,90–94].

Regarding the mechanism of crystal nucleation and growth, we mention that in a very recent work [95] it has been proposed that crystallization is triggered by a pre-ordering of the face-centered-cubic (fcc) sublattice of the Te atoms that precedes the ordering of the square rings of Ge-Te bonds. This picture was inferred from the analysis of the temperature/time dependence of the Te-Te coordination numbers (first neighbors on the anionic fcc sublattice) obtained from the fitting of

Table 8
Crystal growth velocities v_g of overcritical nuclei at 500 K or 600 K in the different models. Homogeneous GeTe refers to simulations S1 and S2 (Table 7). Phase separated Ge_2Te refers to the crystallization after phase separation at 600 K (simulation S3 in Table 7). Homogeneous Ge_2Te refers to the crystallization before phase separation at 500 K (simulation S4 in Table 7).

	v_g (m/s)	
	500 K	600 K
Homogeneous GeTe	1.2	4.5
Phase separated Ge_2Te		3.1
Homogeneous Ge_2Te	0.16	

extended X-ray absorption fine structure (EXAFS) spectrum at the Te K-edge. To check this picture, we computed the Q_6^{dot} order parameter, suited for an fcc lattice, for the separated Te and Ge sublattices. We considered the Te-Te or Ge-Ge coordination on each fcc sublattice for distances up to 4.4 Å which is slightly above the nearest neighbor distance on the fcc sublattice. The distribution of the Q_6^{dot} order parameter for Ge and Te atoms in the cubic β-phase at 600 and 500 K is shown in Fig. S1 in the Supplementary Material. Notice that in the β-phase the Q_6^{dot} distribution is broader for Ge than for Te atoms because of the disorder induced by the Peierls distortion which is randomly aligned along all equivalent <111> directions (see Section 3.1.3). A pre-ordering of the Te fcc sublattice should then result into an increase in the number of crystalline Te atoms assigned by the Q_6^{dot} order parameter for Te before crystallinity would be detected by the Q_6^{dot} order parameter for Ge. The evolution in time of the crystalline Te and Ge atoms assigned by the Q_6^{dot} parameters is shown in Fig. S6 in the Supplementary Material for the crystallization of amorphous GeTe at 600 and 500 K. No delay is observed in the onset of the growth of crystallinity for Te atoms than for Ge atoms which means that there is no pre-ordering of the Te fcc sublattice. We remark, however, that the experimental analysis in Ref. [95] was performed at 440 K on a transformation occurring on the time scale of one hour, while our analysis addresses the nucleation and growth occurring on the time scale of hundreds of ps at 500–600 K. Therefore, we cannot exclude that pre-ordering of the Te fcc sublattice could take place at the experimental conditions mentioned above, albeit according to our results this process does not seem to occur at the operation conditions of PCMs. For our purpose, we considered this validation sufficient to move to the study of the crystallization in Ge_2Te which is discussed hereafter.

3.2.2. Ge_2Te

As mentioned in Section 1, crystallization of the $Ge_{63}Te_{37}$ alloy deposited by magnetron sputtering was studied by several means in Ref. [43]. There, it was found that the crystallization process consists of three separate steps: first, Ge segregates by forming a-Ge regions followed by the crystallization of GeTe and later of pure Ge. These evidences resulted from time resolved measurements of optical reflectivity, X-ray diffraction and Raman spectra during an annealing ramp (0.1 K/s) [43]. The transformation starts at about 600 K, GeTe crystallization was observed at about 630 K, while crystalline Ge appears at an even later time at about 650 K. The crystallized sample
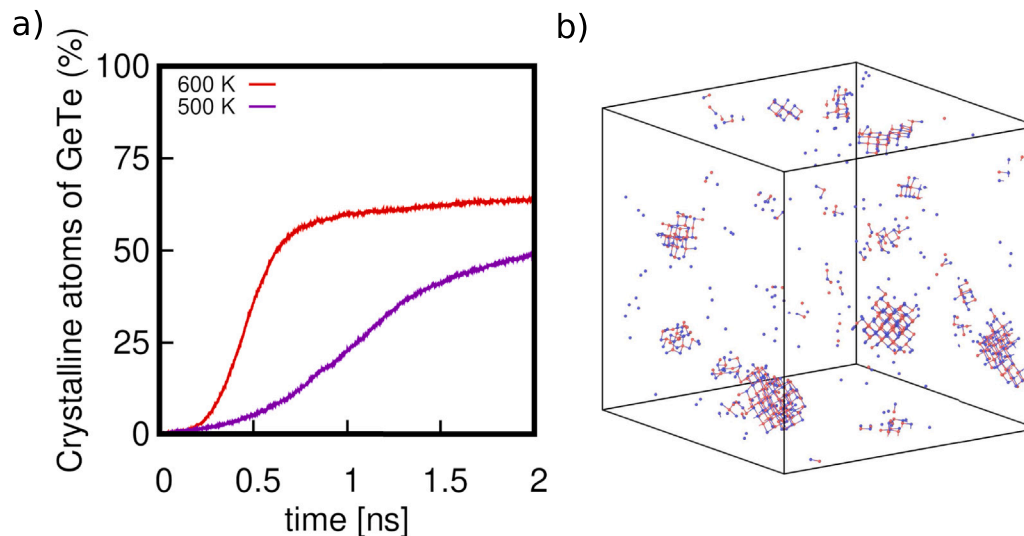
a)

b)

Fig. 8. (a) Fraction of crystalline atoms (defined by Q_4^{dot}) as a function of time in a 32768-atom model of GeTe in simulations at 500 and 600 K. (b) Snapshot of the crystalline atoms in the 32768-atom model of GeTe after 100 ps at 600 K.

was also re-amorphized by laser melting and the resulting amorphous sample crystallizes at the same temperature of the asdep one. In another work [96], a longer crystallization time of about one order of magnitude was reported instead for asdep $Ge_{62}Te_{38}$ sample than for the melt quenched one. This difference was ascribed to the presence of an amorphous-crystal interface in the laser melted sample which favors crystal growth without the need of crystal nucleation [96]. Another Raman study also confirms a multistep crystallization process for $Ge_{76}Te_{24}$ and $Ge_{62}Te_{38}$ [44] where GeTe crystallites were detected at 470 K in $Ge_{62}Te_{38}$ whereas pure Ge crystallizes at a later time at 650 K [44]. A similar behavior was reported from time-resolved diffraction measurements in Ref. [45] for $Ge_{62}Te_{38}$ and in Ref. [46] for $Ge_{62}Sb_{38}$ and $Ge_{69}Sb_{31}$. However, the possibility of the formation of large a-Ge region due to Ge segregation prior to crystal nucleation of GeTe, was not discussed explicitly in Refs. [44–46]. A simultaneous crystallization of GeTe and Ge was reported instead at high temperature of 620 K for $Ge_{70}Te_{30}$ in Ref. [45] under an annealing ramp of 1 K/s. The reason behind the discrepancies among different reports is unclear. Different degree of homogeneity of the alloy under different preparation conditions or different levels of surface oxidation may affect the crystallization temperature. Indeed, oxidation was shown to sizeably lower T_x in GeTe [97] and in Ge-rich GST alloys [98].

On these premises, we started our analysis by first simulating Ge_2Te at the two different temperature 600 K and 500 K in a 30000-atom model at the theoretical amorphous density of 0.0355 atom/$Å^3$ (see Section 3.1.1). By assuming that Ge would segregate as a-Ge at the experimental density of 0.0438 atom/$Å^3$, a phase separation of Ge_2Te at constant volume and at the average density of 0.0355 atom/$Å^3$ would lead to GeTe regions at the density of 0.0326 atom/$Å^3$ which is sufficiently close to the experimental density of a-GeTe of 0.0333 atom/$Å^3$ [89]. Therefore, all simulations were performed at constant volume which is also closer to the operation conditions of PCMs. We chose an orthorhombic cell with edges a=b= 101.82 Å and c= 81.45 Å. The model was equilibrated first at 2000 K for 10 ps and at 1200 K for 40 ps and then quenched to 600 K in 60 ps. At this temperature we performed a NVT simulation lasting 25 ns (simulation S3 in Table 7).

At 600 K, Ge atoms immediately start to segregate from Ge_2Te. Phase separation occurs because the sum of the free energies of GeTe and Ge is lower than that of Ge_2Te in the amorphous of supercooled liquid phases. Indeed, we verified that the reaction energy of the transformation $Ge_2Te \rightarrow GeTe + Ge$ at 600 K is $\Delta E = 6 \pm 2$ meV/atom, as obtained from 6 independent simulations of supercooled liquid models of these compositions at 600 K. Although we did not attempt

to estimate the reaction entropy, the results above confirm that Ge_2Te is unstable against phase separation. To quantify the fraction of segregated Ge atoms, we computed the SOAP similarity kernel k_j for a-Ge as described in Section 2. SOAP k_j for a Ge atom is close to one for configurations similar to the average local configuration in a-Ge and it decreases by increasing the dissimilarity with a-Ge. The distribution of k_j at the beginning of the simulation (t = 0 ns) and after 21 ns is compared in Fig. 9a to the distribution k_j of a-Ge at the same temperature. We could qualitatively assess that a Ge atom is segregated when its SOAP k_j is higher than 0.92, as the distribution of k_j in a-Ge ranges from 0.92 to 1. In the simulation of Ge_2Te, the k_j distribution initially features a single broad peak at around 0.85, while after 21 ns two peaks are present at 0.6 and at 0.95 which highlights the occurrence of a phase separation.

The segregation of Ge is very clear in the snapshots reported in Fig. 9b where we show only Ge atoms in an environment close to a-Ge ($k_j > 0.92$) at the beginning of the simulation and after 21 ns. As shown in Fig. 10a the number of segregated Ge atoms increases initially very fast and then more slowly, reaching a fraction of 30% after 21 ns. Complete phase separation into Ge and GeTe would correspond to a fraction of 50% of segregated Ge atoms.

Segregation of Ge leads to the formation of Ge-rich regions with $Ge_{87}Te_{13}$ composition and average density of 0.041 atom/$Å^3$, and of Ge-poor regions with $Ge_{54}Te_{46}$ composition and average density of 0.03267 atom/$Å^3$ which is very close to the experimental density of the amorphous phase of stoichiometric GeTe (0.0333 atom/$Å^3$). The composition of the Ge-poor region was computing by averaging over about 4000 atoms in a region at least 10 Å far from the region of segregated Ge (see Fig. 9b). Similarly, the composition of the Ge-rich region was computed by averaging over about 3000 atoms in the upper part of the a-Ge-like region (see Fig. 9b).

In the process of formation of the a-Ge regions, Ge atoms is the most diffusing specie as one would envisage from the diffusion coefficients in Fig. 4. The overall average MSD over 10 ns for each species is indeed very close to the value given by the Einstein relation. At 600 K the square root of the average MSD after 10 ns is about 8.1 nm for Ge atoms and about 5.9 nm for Te atoms. We remark that the edge of the simulation cell is 8.1 nm.

Although most of Ge atoms in excess is segregated, we had to wait 21 ns to see the formation of an overcritical nucleus of crystalline GeTe. Once formed, the crystallite grows until the crystal percolates through the simulation box as shown in Fig. 10, but at a lower rate compared to stoichiometric GeTe at the same temperature, as shown in Table 8. At
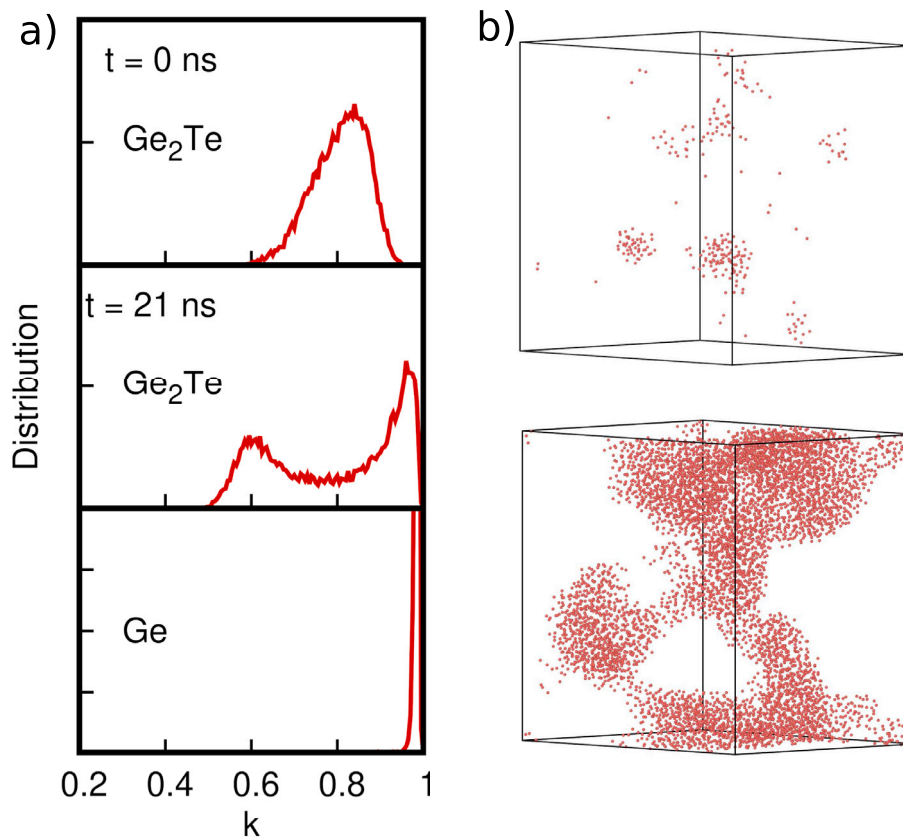
Fig. 9. (a) Distribution of the SOAP k_j at the beginning (top, t = 0 ns) and after 21 ns (center) in the simulation of Ge_2Te at 600 K compared to the distribution of an independent model of a-Ge at the same temperature (bottom). (b) Snapshots of Ge_2Te at the beginning (upper) and after 21 ns (lower) at 600 K. Only atoms with an environment close to that of a-Ge are shown (SOAP $k_j > 0.92$).
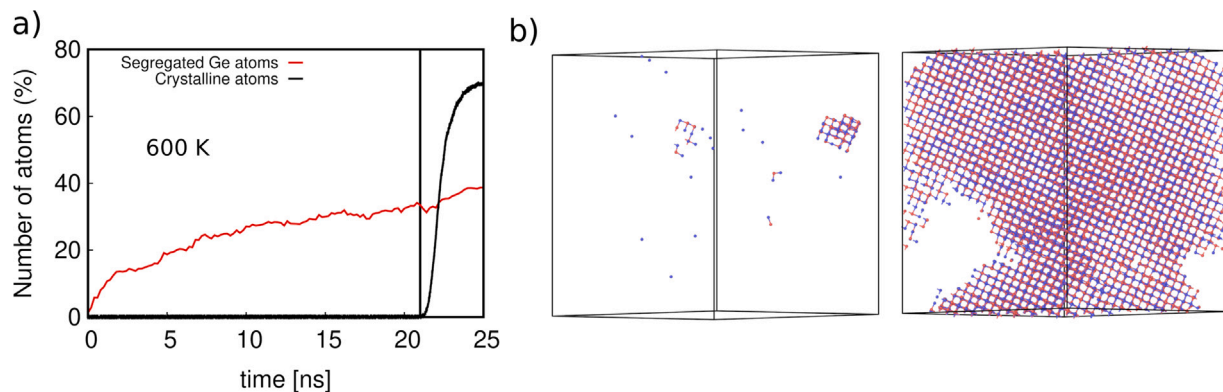

Fig. 10. (a) Number of segregated Ge atoms ($k_j > 0.92$, red line) and fraction of crystalline atoms (defined by Q_4^{dot}, black line) and as a function of time. (b) Crystalline atoms in the segregated large model (30000 atoms) of Ge_2Te at t = 21.5 ns (left) and at t= 25 ns (right) at 600 K. (For interpretation of the references to color in this figure legend, the reader is referred to the web version of this article.)

600 K, the crystal growth velocity is lower in Ge_2Te because a further segregation of Ge must take place during the crystal growth in region with average composition of $Ge_{54}Te_{46}$. The average composition of the crystallized region is in fact $Ge_{50}Te_{50}$. An example of the evolution in time of the radius of a crystalline nucleus at 600 K is shown in Fig. S5 in the Supplementary Material.

We remark that the a-Ge regions remain amorphous after crystallization of GeTe at 600 K.

We also repeated a simulation at 600 K for a homogeneous system (19200 atom) with composition $Ge_{54}Te_{46}$ generated by quenching from the melt (simulation S8 in Table 7) and we similarly observed the formation of one crystalline nucleus after 8 ns. The crystal growth velocity is the same of that obtained for the phase separated system, as given in Table 8.

To assess if the system might undergo phase separation also at lower temperatures, we quenched the liquid model from 1200 K to 500 K in 70 ps and we then performed a NVT simulation at this temperature for 10 ns (simulation S4 in Table 7). The percentage of segregated Ge atoms reaches only 4% after 10 ns, as shown in Fig. 11. We can conceive that the system does not segregate in Ge_2Te at 500 K due to the lower atomic mobility of Ge atoms at this temperature. The diffusion coefficient as a function of temperature, shown in Fig. 4, features a super-Arrhenius behavior with a drop from $1 \cdot 10^{-5}$ cm^2/s at 600 K to $0.85 \cdot 10^{-6}$ cm^2/s at 500 K. However, the slow down with temperature of the kinetics of Ge segregation is not simply due to the decrease of the growth velocity of the a-Ge regions. Would this be the case, we should see an increase in the growth time of a-Ge at 500 K with respect to 600 K equal to the ratio of the diffusion coefficients, if we consider an Avrami theory
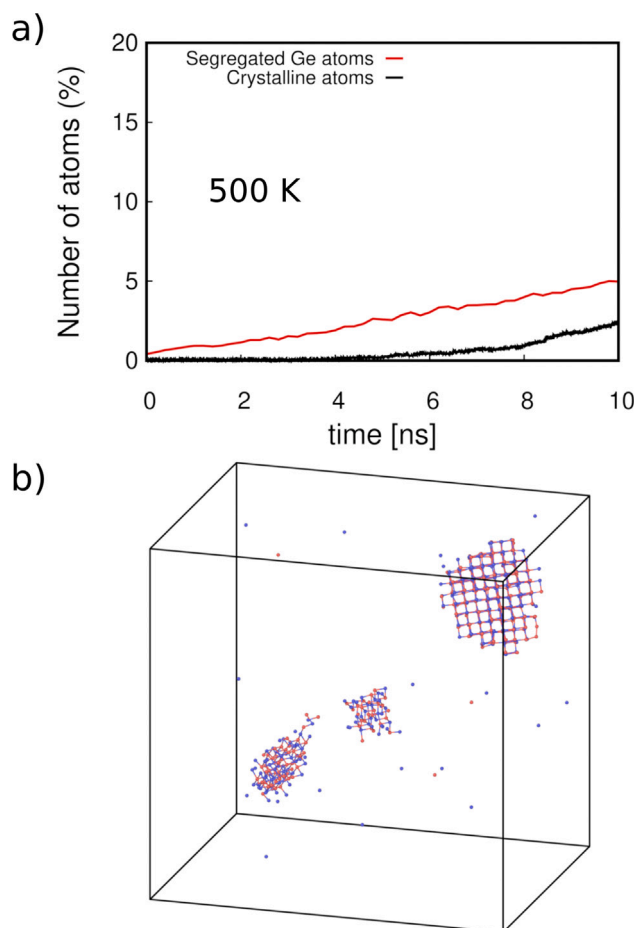
a)

b)

Fig. 11. (a) Number of segregated Ge atoms ($k_j > 0.92$, red line) and fraction of crystalline atoms (defined by Q_4^{dot}, black line) and as a function of time in the simulation of Ge$_2$Te at 500 K. (b) Crystal nucleation was observed before phase separation. Snapshot of the crystalline nuclei at 10 ns. (For interpretation of the references to color in this figure legend, the reader is referred to the web version of this article.)

a)

b)

c)

Fig. 12. Evolution in time of the internal energy per atom for (a) stoichiometric GeTe at 600 K (32768-atom cell), Ge$_2$Te (30000-atom cell) at (b) 600 K and (c) at 500 K. Vertical lines in panel (c) indicate the onset of crystallization.

with just the growth of pre-formed nuclei [99]. From Figs. 10–11 we note that 4% of segregated atoms is reached in 0.3 ns at 600 K and in 10 ns at 500 K, while one would expect to see the same fraction after 3.4 ns at 500 k from the scaling by the ratio of the diffusion coefficients ($D_{600}/D_{500} = 11.8$). In fact, while at 600 K we see the formation of overcritical nuclei of a-Ge like in the time span of fraction of ns, at 500 K no overcritical nuclei of a-Ge form in 10 ns. Therefore nucleation of a-Ge region seems to control the kinetic of phase separation.

Despite the lack of a-Ge segregation, we observed after 6 ns the formation of a single overcritical nucleus of crystalline GeTe that grew very slowly by expelling the excess of Ge. Surprisingly, crystal nucleation occurred without prior phase segregation in a region where the local content of Ge-Ge bonds is lower than the average in the Ge$_2$Te homogeneous model and also lower than the average of homogeneous GeTe. A snapshot of the distribution of Ge atoms with a fraction of Ge-Ge bonds lower than the average in a-GeTe (0.79) is shown in Fig. S7 in the Supplementary Material. The crystal growth velocity is low as shown in Table 8 because of the need of expel a large amount of Ge. The evolution in time of the number of crystalline atoms in the simulation at 500 K and a snapshot of the overcrictical crystalline nucleus are shown in Fig. 11.

The dependence of the nucleation time on the different simulation conditions can be seen in Fig. 12 where the internal energy is reported as a function of time. A sudden drop of the internal energy corresponds to the onset of crystallization in GeTe and in Ge$_2$Te at 600 K. At
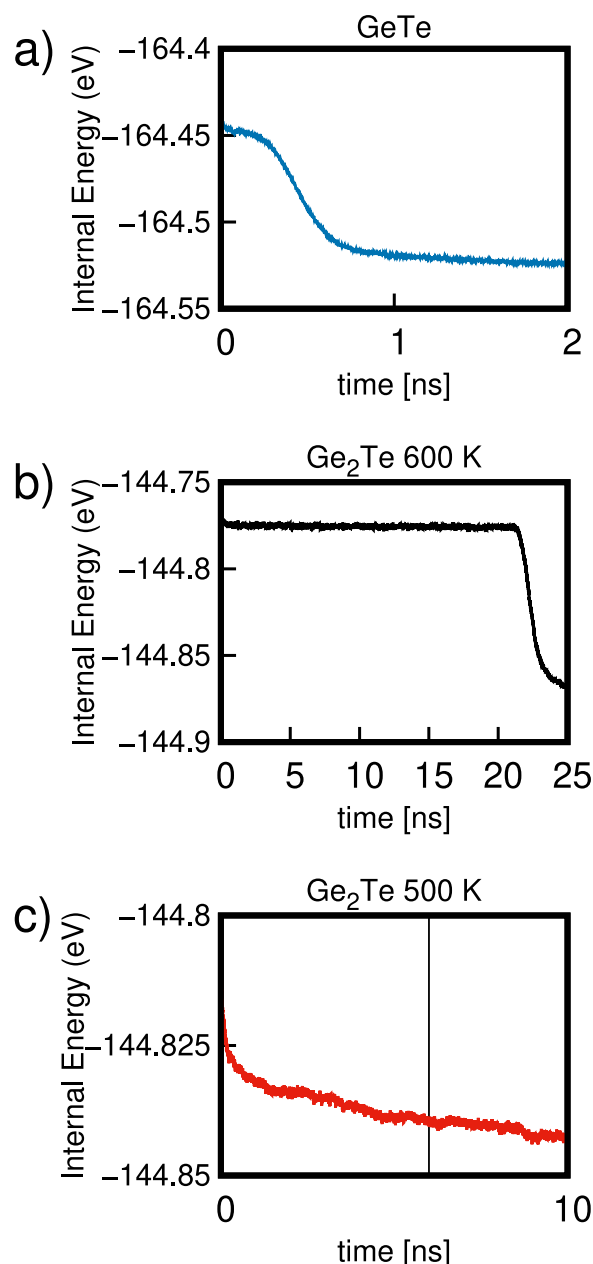
500 K the crystal growth is slow and the decrease in energy due to crystallization superimposes to the effect due to equilibration of the supercooled liquid which is slow as well for the off-stoichiometric system at this temperature.

We have also studied the crystallization at 600 K and 500 K of an amorphous 30000-atom model generated by quenching from 1200 K to 300 K in 100 ps and then annealed abruptly at the two target temperatures (simulations S5 and S6 in Table 7). The results are similar to those of the liquid model supercooled from the melt discussed above. The overheated amorphous phase crystallizes concurrently with the phase separation at 500 K, while phase segregation precedes crystal nucleation at 600 K. The evolution in time of the fraction of segregated atoms and of the fraction of crystalline atoms for this last model at 500 and 600 K are shown in Fig. S8 in the Supplementary Material.

Therefore, we have observed two different regimes at different temperatures. At high temperature (600 K), the nucleation time of a-Ge is very short and phase separation with segregation of most of Ge in excess was observed to occur in a few ns. This yields a GeTe-like region with composition $Ge_{54}Te_{46}$ where the nucleation time for crystalline GeTe is several ns in a 30000-atom cell, to be compared with the value of a few hundreds of ps in stoichiometric GeTe at the same temperature and for a similar cell size (32768 atoms). At 600 K, phase separation was observed to occur first and GeTe crystallization follows in a two steps mechanism. At lower temperatures (500 K), phase separation does not occur on the time scale of our simulations because the overcritical nuclei of a-Ge do not form, albeit Ge is still very mobile. Still, nucleation of crystalline GeTe is possible at 500 K without phase separation, but with a low crystal growth velocity because Ge in excess must be expelled during growth. At 500 K, crystallization was observed to take place as a single step process with Ge segregation occurring simultaneously with the growth of GeTe crystallites. We remark that all the features described so far for the crystallization of Ge_2Te were also reproduced in the simulation of a second 30000-atom model and of a smaller 19200-atom model with the first NN potential fitted on the database including Ge, GeTe and Ge_2Te only. The nucleation time of this second set of simulations was also on the same timescale of those reported above, although the actual values were obviously different being the nucleation a stochastic process. In this respect, a word of caution is needed on the conclusions on the crystallization kinetics that we have just drawn. The phenomenology that we have just described is based on a few brute-force simulations of the crystallization process that are not sufficient to provide a quantitative estimate of the nucleation rates or nucleation times. This would be possible in principle by exploiting more sophisticated statistical mechanics tools such as the forward flux sampling (FFS) method [100,101] that has been used for several systems within classical MD simulations. This approach provides directly a steady state nucleation rate which is particularly suitable for materials in which the small size of the critical nucleus (40–50 atoms at 500–600 K in GeTe and GST [37,62]) makes the application of classical nucleation theory (CNT) [101–103] questionable. However, FFS is still quite computationally demanding also for NN simulations. Moreover, the crystallization under the conditions of memory operation may occur in a transient regime before reaching the steady nucleation rate because of the fast raise in temperature and of the small size of the active region in the actual devices. Therefore, although we do not exclude to use paths sampling methods in the near future, in the present work we limited ourselves to a few simulations of the nucleation events that we believe provide some useful information, in spite of the lack of statistics in the nucleation times. Since the phase separation at 600 K is much faster that crystal nucleation in all the simulations (with the first and final version of the NN potential), we are confident to conclude that phase separation is likely to precede crystal nucleation in the operation of the real device at 600 K. Secondly, in all simulations at 500 K (with the first and final version of the NN potential) we did not observe phase separation prior to crystal nucleation which supports our claim of a different kinetics at lower temperature.

We remark, moreover, that the segregation process is reversible. In fact, a homogeneous Ge_2Te liquid alloy is recovered by heating the system above the liquid temperature of 1150 K. This was shown by first equilibrating at 300 K the phase-separated and crystallized model generated at 600 K, and then by heating the system at 1200 K for 0.8 ns (simulation S7 in Table 7). The re-homogenization of the system was monitored by computing the number of segregated atoms with the k_j descriptor which is now tuned on liquid Ge at the target temperature of 1200 K. The evolution with time of the number of segregated atoms after raising the temperature from 300 K to 1200 K is shown in Fig S9 in the Supplementary Material.

We attempt now to make a contact with the experimental results of Refs. [43–45]. The single step crystallization that we see at 500 K seems consistent with the crystallization seen in Refs. [44,45] at 470 K. We

must remark, however, that our models are generated by quenching from the melt which corresponds to the operation conditions of the memory devices, while in Refs. [44,45] crystallization was studied experimentally in the asdep samples. On the other hand, the two steps crystallization we see at 600 K, seems consistent with the two steps process (first segregation of Ge and then crystallization of GeTe) seen in Ref. [43] at 600–630 K. Our simulations cannot, however, explain why a single step crystallization at a lower temperature of 500 K was not seen in Ref. [43]. We cannot exclude that our NN potential could overestimate the nucleation rate of GeTe, as it seems to occur [104] for the NN potential for stoichiometric GeTe that we developed previously [35].

4. Conclusions

In summary, we have generated a machine-learned potential for Ge-rich Ge_xTe binary alloy by using the NN method implemented in the DeePMD package. We assessed that the NN potential can accurately reproduce the structural properties of the amorphous, liquid, and crystalline phases of Ge, GeTe, Ge_2Te and more Ge-rich Ge_xTe alloys. Then, this potential was used to study the crystallization mechanism of Ge_2Te by MD simulations of 30000-atom cells lasting more than 20 ns. In stoichiometric GeTe, the system crystallizes in a few ns at both 600 and 500 K, consistently with previous simulations in literature [62]. For Ge_2Te, although we do not have enough statistics to reliably estimate the nucleation time, we believe that we can safely draw some conclusions on the presence of a different crystallization behavior at different temperatures. At 500 K, we saw the formation of a crystalline nucleus of GeTe before phase separation. Nucleation starts in a point where the fraction of Ge-Ge bonds is lower than the average of stoichiometric a-GeTe. Crystal growth is, however, slow as all Ge in excess must be expelled during growth. At this temperature, overcritical a-Ge nuclei was not observed on the time scale of 10 ns if not preempted by crystal nucleation. On the contrary, at 600 K phase separation was observed to take place first with the formation of large and separated regions with average compositions $Ge_{87}Te_{13}$ and $Ge_{54}Te_{46}$. The slow down with temperature of the segregation process seems to be due to the increase of the time needed for the formation of overcritical nuclei of a-Ge. Crystallization then occurs at 600 K in the Ge-poor region with a nucleation time still much longer than that of stoichiometric GeTe. Once a supercritical nucleus is formed in $Ge_{54}Te_{46}$ regions, crystal growth proceeds with a further expulsion of Ge in excess (because of a larger driving force for Ge segregation in the crystalline phase) which, however, implies a still lower crystal growth velocity with respect to stoichiometric GeTe. We remark that the a-Ge regions remain amorphous after crystallization of GeTe at 500 and 600 K on the time scale of our simulations.

Overall, our simulations represent a first step towards the atomistic modeling of the crystallization in Ge-rich GeSbTe alloys which are of interest for applications in embedded memories. Firstly, we have shown that it is possible to devise a reliable NN potential suitable to describe the full range of composition from Ge_2Te to GeTe and pure Ge. The database that we generated for this purpose will contribute to the training set for the development of a NN potential for the Ge-rich GeSbTe alloys which is in progress. Secondly, we have shown that phase separation with segregation of most of Ge in excess occurs on the relatively short time scale of a few ns in Ge_2Te at high temperature (600 K). The complex process of Ge segregation and crystallization in non-stoichiometric alloys can thus be tackled by MD simulations.

CRediT authorship contribution statement

Dario Baratella: Writing – review & editing, Writing – original draft, Visualization, Validation, Software, Resources, Investigation, Formal analysis, Data curation. **Omar Abou El Kheir:** Writing – review & editing, Software, Methodology. **Marco Bernasconi:** Writing – review & editing, Writing – original draft, Validation, Supervision, Project administration, Methodology, Investigation, Funding acquisition, Formal analysis, Data curation, Conceptualization.

Declaration of competing interest

The authors declare that they have no known competing financial interests or personal relationships that could have appeared to influence the work reported in this paper.

Acknowledgments

Code availability

LAMMPS, DeePMD and CP2k are free and open source codes available at https://lammps.sandia.gov, http://www.deepmd.org and http://www.cp2k.org, respectively.

Appendix A. Supplementary material

Supplementary material related to this article can be found online at https://doi.org/10.1016/j.actamat.2024.120608.

Data availability

The NN potential, the training DFT database, atomic trajectories of the phase separation and crystallization process, and a video of the relevant processes are available in the Materials Cloud repository at https://doi.org/10.24435/materialscloud:cf-tq.

References

[1] M. Wuttig, N. Yamada, Phase-change materials for rewriteable data storage, Nature Mater. 6 (11) (2007) 824.

[2] P. Noé, C. Vallée, F. Hippert, F. Fillot, J.-Y. Raty, Phase-change materials for non-volatile memory devices: from technological challenges to materials science issues, Semicond. Sci. Technol. 33 (1) (2018) 013002.

[3] W. Zhang, R. Mazzarello, M. Wuttig, E. Ma, Designing crystallization in phase-change materials for universal memory and neuro-inspired computing, Nat. Rev. Mater. 4 (3) (2019) 150.

[4] A. Pirovano, A. Lacaita, A. Benvenuti, F. Pellizzer, R. Bez, Electronic switching in phase-change memories, IEEE Trans. Electron Devices 51 (2004) 452–459.

[5] J. Choe, Intel 3D XPoint Memory Die Removed from Intel Optane^{TM} PCM (Phase Change Memory), 2017, URL https://www.techinsights.com/blog/intel-3d-xpoint-memory-die-removed-intel-optanetm-pcm-phase-change-memory. (Accessed 23 April 2024).

[6] P. Cappelletti, R. Annunziata, F. Arnaud, F. Disegni, A. Maurelli, P. Zuliani, Phase change memory for automotive grade embedded NVM applications, J. Phys. D: Appl. Phys. 53 (19) (2020) 193002.

[7] A. Redaelli, E. Petroni, R. Annunziata, Material and process engineering challenges in Ge-rich GST for embedded PCM, Mater. Sci. Semicond. Process. 137 (2022) 106184.

[8] P. Noé, C. Sabbione, N. Bernier, N. Castellani, F. Fillot, F. Hippert, Impact of interfaces on scenario of crystallization of phase change materials, Acta Mater. 110 (2016) 142–148.

[9] Y. Kim, U. Hwang, Y.J. Cho, H. Park, M.-H. Cho, P.-S. Cho, J.-H. Lee, Change in electrical resistance and thermal stability of nitrogen incorporated $Ge_2Sb_2Te_5$ films, Appl. Phys. Lett. 90 (2) (2007) 021908.

[10] E.T. Kim, J.Y. Lee, Y.T. Kim, Investigation of electrical characteristics of the $In_3Sb_1Te_2$ ternary alloy for application in phase-change memory, Phys. Status Solidi RRL 3 (4) (2009) 103.

[11] H.-Y. Cheng, S. Raoux, J.L. Jordan-Sweet, The crystallization behavior of stoichiometric and off-stoichiometric Ga–Sb–Te materials for phase-change memory, Appl. Phys. Lett. 98 (12) (2011) 121911.

[12] T. Morikawa, K. Kurotsuchi, M. Kinoshita, N. Matsuzaki, Y. Matsui, Y. Fujisaki, S. Hanzawa, A. Kotabe, M. Terao, H. Moriya, et al., Doped In-Ge-Te phase change memory featuring stable operation and good data retention, in: 2007 IEEE International Electron Devices Meeting, IEEE, 2007, pp. 307–310.

[13] H.Y. Cheng, T.H. Hsu, S. Raoux, J. Wu, P.Y. Du, M. Breitwisch, Y. Zhu, E.K. Lai, E. Joseph, S. Mittal, R. Cheek, A. Schrott, S.C. Lai, H.L. Lung, C. Lam, A high performance phase change memory with fast switching speed and high temperature retention by engineering the $Ge_xSb_yTe_z$ phase change material, in: 2011 International Electron Devices Meeting, 2011, p. 3.4.1.

[14] P. Zuliani, E. Varesi, E. Palumbo, M. Borghi, I. Tortorelli, D. Erbetta, G.D. Libera, N. Pessina, A. Gandolfo, C. Prelini, L. Ravazzi, R. Annunziata, Overcoming temperature limitations in phase change memories with optimized $Ge_xSb_yTe_z$, IEEE Trans. Electron Devices 60 (2013) 4020.

[15] P. Zuliani, E. Palumbo, M. Borghi, G. Dalla Libera, R. Annunziata, Engineering of chalcogenide materials for embedded applications of phase change memory, Solid State Electron. 111 (2015) 27.

[16] E. Palumbo, P. Zuliani, M. Borghi, R. Annunziata, Forming operation in Ge-rich $Ge_xSb_yTe_z$ phase change memories, Solid State Electron. 133 (2017) 38.

[17] G. Navarro, M. Coué, A. Kiouseloglou, P. Noé, F. Fillot, V. Delaye, A. Persico, A. Roule, M. Bernard, C. Sabbione, et al., Trade-off between SET and data retention performance thanks to innovative materials for phase-change memory, in: 2013 IEEE International Electron Devices Meeting, IEEE, 2013, p. 21.5.1.

[18] V. Sousa, G. Navarro, N. Castellani, M. Coue, O. Cueto, C. Sabbione, P. Noe, L. Perniola, S. Blonkowski, P. Zuliani, et al., Operation fundamentals in 12Mb phase change memory based on innovative Ge-rich GST materials featuring high reliability performance, in: 2015 Symposium on VLSI Technology, VLSI Technology, 2015, p. T98.

[19] F. Arnaud, P. Ferreira, F. Piazza, A. Gandolfo, P. Zuliani, P. Mattavelli, E. Gomiero, G. Samanni, J. Jasse, C. Jahan, J.P. Reynard, R. Berthelon, O. Weber, A. Villaret, B. Dumont, J.C. Grenier, R. Ranica, C. Gallon, C. Boccaccio, A. Souhaite, L. Desvoivres, D. Ristoiu, L. Favennec, V. Caubet, S. Delmedico, N. Cherault, R. Beneyton, S. Chouteau, P.O. Sassoulas, L. Clement, P. Boivin, D. Turgis, F. Disegni, J.L. Ogier, X. Federspiel, O. Kermarrec, M. Molgg, A. Viscuso, R. Annunziata, A. Maurelli, P. Cappelletti, E. Ciantar, High density embedded PCM cell in 28 nm FDSOI technology for automotive micro-controller applications, in: 2020 IEEE International Electron Devices Meeting, IEDM, 2020, pp. 24.2.1–24.2.4.

[20] A. Kiouseloglou, G. Navarro, V. Sousa, A. Persico, A. Roule, A. Cabrini, G. Torelli, S. Maitrejean, G. Reimbold, B. De Salvo, F. Clermidy, L. Perniola, A novel programming technique to boost low-resistance state performance in Ge-rich GST phase change memory, IEEE Trans. Electron Devices 61 (2014) 1246.

[21] N. Grossier, F. Disegni, A. Ventre, A. Barcella, R. Mariani, V. Marino, S. Mazzara, A. Scavuzzo, M. Bansal, B. Soni, A. Anand, S. Banzal, D. Joshi, R. Narwal, M. Niranjani, K. Trivedi, P. Ferreira, R. Ranica, L. Vullo, A. Cathelin, A. Maurelli, S. Pezzini, M. Peri, ASIL-D automotive-grade microcontroller in 28 nm FD-SOI with full-OTA capable 21MB embedded PCM memory and highly scalable power management, in: 2023 IEEE Symposium on VLSI Technology and Circuits, VLSI Technology and Circuits, 2023, pp. 1–2.

[22] M. Agati, M. Vallet, S. Joulié, D. Benoit, A. Claverie, Chemical phase segregation during the crystallization of Ge-rich GeSbTe alloys, J. Mater. Chem. C 7 (28) (2019) 8720.

[23] M.A. Luong, M. Agati, N. Ratel Ramond, J. Grisolia, Y. Le Friec, D. Benoit, A. Claverie, On some unique specificities of Ge-rich GeSbTe phase-change material alloys for nonvolatile embedded-memory applications, Phys. Status Solidi RRL 15 (3) (2021) 2000471.

[24] E. Rahier, M.-A. Luong, S. Ran, N. Ratel-Ramond, S. Saha, C. Mocuta, D. Benoit, Y. Le-Friec, A. Claverie, Multistep crystallization of Ge-rich GST unveiled by in situ synchrotron X-ray diffraction and (scanning) transmission electron microscopy, Phys. Status Solidi RRL 17 (2023) 2200450.

[25] S. Privitera, V. Sousa, C. Bongiorno, G. Navarro, C. Sabbione, E. Carria, E. Rimini, Atomic diffusion in laser irradiated Ge rich GeSbTe thin films for phase change memory applications, J. Phys. D: Appl. Phys. 51 (2018) 145103.

[26] S. Privitera, I. López García, C. Bongiorno, V. Sousa, M. Cyrille, G. Navarro, C. Sabbione, E. Carria, E. Rimini, Crystallization properties of melt-quenched Ge-rich GeSbTe thin films for phase change memory applications, J. Appl. Phys. 128 (2020) 155105.

[27] L. Prazakova, E. Nolot, E. Martinez, D. Rouchon, F. Fillot, N. Bernier, R. Elizalde, M. Bernard, G. Navarro, The effect of Ge content on structural evolution of Ge-rich GeSbTe alloys at increasing temperature, Materialia 21 (2022) 101345.

[28] A. Díaz Fattorini, C. Chèze, I. Lø'pez García, C. Petrucci, M. Bertelli, F. Righi Riva, S. Prili, S.M.S. Privitera, M. Buscema, A. Sciuto, S. Di Franco, G. D'Arrigo, M. Longo, S. De Simone, V. Mussi, E. Placidi, M.-C. Cyrille, N.-P. Tran, R. Calarco, F. Arciprete, Growth, Electronic and electrical characterization of Ge-rich Ge–Sb–Te alloy, Nanomaterials 12 (2022) 1340.

[29] S. Cecchi, I. Lopez Garcia, A.M. Mio, E. Zallo, O. Abou El Kheir, R. Calarco, M. Bernasconi, G. Nicotra, S.M. Privitera, Crystallization and electrical properties of Ge-rich GeSbTe alloys, Nanomaterials 12 (4) (2022) 631.

[30] L. Laurin, M. Baldo, E. Petroni, G. Samanni, L. Turconi, A. Motta, M. Borghi, A. Serafini, D. Codegoni, M. Scuderi, S. Ran, A. Claverie, D. Ielmini, R. Annunziata, A. Redaelli, Unveiling retention physical mechanism of Ge-rich GST ePCM technology, in: 2023 IEEE International Reliability Physics Symposium, IRPS, 2023, pp. 1–7.

[31] E. Petroni, A. Serafini, D. Codegoni, P. Targa, L. Mariani, M. Scuderi, G. Nicotra, A. Redaelli, Metrics for quantification of by-process segregation in Ge-rich GST, Front. Phys. 10 (2022) 862954.

[32] E. Petroni, M. Patelmo, A. Serafini, D. Codegoni, L. Laurin, M. Baldo, A. Redaelli, Advanced metrics for quantification of by-process segregation beyond ternary systems, Phys. Status Solidi RRL 17 (2023) 2200458.

[33] L. Sun, Y.-X. Zhou, X.-D. Wang, Y.-H. Chen, V.L. Deringer, R. Mazzarello, W. Zhang, Ab initio molecular dynamics and materials design for embedded phase-change memory, npj Comput. Mater. 7 (1) (2021) 29.

[34] O. Abou El Kheir, M. Bernasconi, High-throughput calculations on the decomposition reactions of off-stoichiometry GeSbTe alloys for embedded memories, Nanomaterials 11 (9) (2021) 2382.

[35] G.C. Sosso, G. Miceli, S. Caravati, J. Behler, M. Bernasconi, Neural network interatomic potential for the phase change material GeTe, Phys. Rev. B 85 (2012) 174103.

[36] J. Behler, M. Parrinello, Generalized neural-network representation of high-dimensional potential-energy surfaces, Phys. Rev. Lett. 98 (2007) 146401.

[37] O. Abou El Kheir, L. Bonati, M. Parrinello, M. Bernasconi, Unraveling the crystallization kinetics of the $Ge_2Sb_2Te_5$ phase change compound with a machine-learned interatomic potential, npj Comput. Mater. 10 (2024) 33.

[38] L. Zhang, J. Han, H. Wang, R. Car, W. E, Deep potential molecular dynamics: A scalable model with the accuracy of quantum mechanics, Phys. Rev. Lett. 120 (2018) 143001.

[39] J. Zeng, D. Zhang, D. Lu, P. Mo, et al., DeePMD-kit v2: A software package for deep potential models, J. Chem. Phys. 159 (5) (2023) 054801.

[40] H. Wang, L. Zhang, J. Han, E. Weinan, DeePMD-kit: A deep learning package for many-body potential energy representation and molecular dynamics, Comput. Phys. Comm. 228 (2018) 178.

[41] F.C. Mocanu, K. Konstantinou, T.H. Lee, N. Bernstein, V.L. Deringer, G. Csányi, S.R. Elliott, Modeling the phase-change memory material, $Ge_2Sb_2Te_5$, with a machine-learned interatomic potential, J. Phys. Chem. B 122 (2018) 8998–9006.

[42] Y. Zhou, W. Zhang, E. Ma, V.L. Deringer, Device-scale atomistic modelling of phase-change memory materials, Nat. Electr. 6 (2023) 746–754.

[43] E. Carria, A. Mio, S. Gibilisco, M. Miritello, C. Bongiorno, M. Grimaldi, E. Rimini, Amorphous-crystal phase transitions in Ge_xTe_{1-x} alloys, J. Electrochem. Soc. 159 (2012) H130.

[44] E. Gourvest, S. Lhostis, J. Kreisel, M. Armand, S. Maitrejean, A. Roule, C. Vallée, Evidence of Germanium precipitation in phase-change $Ge_{1-x}Te_x$ thin films by Raman scattering, Appl. Phys. Lett. 95 (3) (2009) 031908.

[45] S. Raoux, B. Muñoz, H.-Y. Cheng, J.L. Jordan-Sweet, Phase transitions in Ge–Te phase change materials studied by time-resolved X-ray diffraction, Appl. Phys. Lett. 95 (14) (2009) 143118.

[46] G. Navarro, V. Sousa, A. Persico, N. Pashkov, A. Toffoli, J.-C. Bastien, L. Perniola, S. Maitrejean, A. Roule, P. Zuliani, R. Annunziata, B. De Salvo, Material engineering of Ge_xTe_{100-x} compounds to improve phase-change memory performances, Solid State Electron. 89 (2013) 93–100.

[47] J. VandeVondele, M. Krack, F. Mohamed, M. Parrinello, T. Chassaing, J. Hutter, Quickstep: Fast and accurate density functional calculations using a mixed Gaussian and plane waves approach, Comput. Phys. Comm. 167 (2) (2005) 103–128.

[48] J.P. Perdew, K. Burke, M. Ernzerhof, Generalized Gradient Approximation Made Simple, Phys. Rev. Lett. 77 (1996) 3865.

[49] S. Goedecker, M. Teter, J. Hutter, Separable dual-space Gaussian pseudopotentials, Phys. Rev. B 54 (1996) 1703.

[50] M. Krack, Pseudopotentials for H to Kr optimized for gradient-corrected exchange–correlation functionals, Theor. Chem. Acc. 114 (2005) 145.

[51] A. Vaswani, N. Shazeer, N. Parmar, J. Uszkoreit, L. Jones, A.N. Gomez, L. u. Kaiser, I. Polosukhin, Attention is all you need, in: I. Guyon, U.V. Luxburg, S. Bengio, H. Wallach, R. Fergus, S. Vishwanathan, R. Garnett (Eds.), Advances in Neural Information Processing Systems, Vol. 30, Curran Associates, Inc., 2017.

[52] A.P. Thompson, H.M. Aktulga, R. Berger, D.S. Bolintineanu, W.M. Brown, P.S. Crozier, P.J. in 't Veld, A. Kohlmeyer, S.G. Moore, T.D. Nguyen, R. Shan, M.J. Stevens, J. Tranchida, C. Trott, S.J. Plimpton, LAMMPS - a flexible simulation tool for particle-based materials modeling at the atomic, meso, and continuum scales, Comp. Phys. Comm. 271 (2022) 108171.

[53] P.J. Steinhardt, D.R. Nelson, M. Ronchetti, Bond-orientational order in liquids and glasses, Phys. Rev. B 28 (1983) 784–805.

[54] P.R. ten Wolde, M.J. Ruiz-Montero, D. Frenkel, Numerical calculation of the rate of crystal nucleation in a lennard-jones system at moderate undercooling, J. Chem. Phys. 104 (1996) 9932.

[55] A.P. Bartók, R. Kondor, G. Csányi, On representing chemical environments, Phys. Rev. B 87 (2013) 184115.

[56] S. De, A.P. Bartók, G. Csányi, M. Ceriotti, Comparing molecules and solids across structural and alchemical space, Phys. Chem. Chem. Phys. 18 (2016) 13754–13769.

[57] F. Musil, A. Grisafi, A.P. Bartók, C. Ortner, G. Csányi, M. Ceriotti, Physics-inspired structural representations for molecules and materials, Chem. Rev. 121 (16) (2021) 9759–9815.

[58] Y. Xu, Y. Zhou, X.-D. Wang, W. Zhang, E. Ma, V.L. Deringer, R. Mazzarello, Unraveling crystallization mechanisms and electronic structure of phase-change materials by large-scale ab initio simulations, Adv. Mat. 34 (11) (2022) 2100139.

[59] J. Laakso, L. Himanen, H. Homm, E.V. Morooka, M.O. Jäger, M. Todorović, P. Rinke, Updates to the DScribe library: New descriptors and derivatives, J. Chem. Phys. 158 (23) (2023) 234802.

[60] L. Himanen, M.O.J. Jäger, E.V. Morooka, F. Federici Canova, Y.S. Ranawat, D.Z. Gao, P. Rinke, A.S. Foster, DScribe: Library of descriptors for machine learning in materials science, Comput. Phys. Comm. 247 (2020) 106949.

[61] A.H. Larsen, et al., The atomic simulation environment — a Python library for working with atoms, J. Phys.: Condens. Matter. 29 (2017) 273002.

[62] G.C. Sosso, G. Miceli, S. Caravati, F. Giberti, J. Behler, M. Bernasconi, Fast crystallization of the phase change compound GeTe by large-scale molecular dynamics simulations, J. Phys. Chem. Lett. 4 (2013) 4241–4246.

[63] S. Urata, Modeling short-range and three-membered ring structures in lithium borosilicate glasses using a machine-learning potential, J. Phys. Chem. C 126 (2022) 21507–21517.

[64] B. Zhai, H. Wang, Accurate interatomic potential for the nucleation in liquid Ti-Al binary alloy developed by deep neural network learning method, Comput. Mater. Sci. 216 (2023) 111843.

[65] J. Liu, R. Liu, Y. Cao, M. Chen, Solvation structures of calcium and magnesium ions in water with the presence of hydroxide: a study by deep potential molecular dynamics, Phys. Chem. Chem. Phys. 25 (2023) 983–993.

[66] X. Huang, K. Luo, Y. Shen, Y. Yue, Q. An, Grain boundaries induce significant decrease in lattice thermal conductivity of CdTe, Energy AI 11 (2023) 100210.

[67] K. Laaziri, S. Roorda, J. Baribeau, Density of amorphous Si_xGe_{1-x} alloys prepared by high-energy ion implantation, J. Non-Cryst. Solids 191 (1995) 193–199.

[68] H. Weber, M. Schumacher, P. Jóvári, Y. Tsuchiya, W. Skrotzki, R. Mazzarello, I. Kaban, Experimental and ab initio molecular dynamics study of the structure and physical properties of liquid GeTe, Phys. Rev. B 96 (2017) 054204.

[69] S. Grimme, J. Antony, S. Ehrlich, H. Krieg, A consistent and accurate ab initio parametrization of density functional dispersion correction (DFT-D) for the 94 elements H-Pu, J. Chem. Phys. 132 (2010) 154104.

[70] G.C. Sosso, J. Behler, M. Bernasconi, Breakdown of Stokes-Einstein relation in the supercooled liquid state of phase change materials, Phys. Status Solidi b 249 (10) (2012) 1880.

[71] W. Klemm, G. Frischmuth, Das system germanium–tellur, Z. Anorg. Allg. Chem. 218 (3) (1934) 249–251.

[72] A. Schlieper, Y. Feutelais, S. Fries, B. Legendre, R. Blachnik, Thermodynamic evaluation of the Germanium — Tellurium system, CALPHAD 23 (1999) 1–18.

[73] B. Dünweg, K. Kremer, Molecular dynamics simulation of a polymer chain in solution, J. Chem. Phys. 99 (1993) 6983–6997.

[74] M.H. Cohen, G. Grest, Liquid-glass transition, a free-volume approach, Phys. Rev. B 20 (3) (1979) 1077.

[75] C.A. Angell, Formation of glasses from liquids and biopolymers, Science 267 (1995) 1924–1935.

[76] S. Imabayashi, M. Ishimaru, Molecular dynamics study on structural relaxation processes in amorphous germanium, Mater. Trans. 58 (2017) 857–861.

[77] Y. Chen, G. Wang, L. Song, X. Shen, J. Wang, J. Huo, R. Wang, T. Xu, S. Dai, Q. Nie, Unraveling the crystallization kinetics of supercooled liquid GeTe by ultrafast calorimetry, Cryst. Growth Des. 17 (2017) 3687–3693.

[78] V.L. Deringer, W. Zhang, M. Lumeij, S. Maintz, M. Wuttig, R. Mazzarello, R. Dronskowski, Bonding nature of local structural motifs in amorphous GeTe, Angew. Chem. Int. Edn 53 (2014) 10817–10820.

[79] J.R. Errington, P.G. Debenedetti, Relationship between structural order and the anomalies of liquid water, Nature 409 (6818) (2001) 318.

[80] R. Mazzarello, S. Caravati, S. Angioletti-Uberti, M. Bernasconi, M. Parrinello, Signature of tetrahedral ge in the Raman spectrum of amorphous phase-change materials, Phys. Rev. Lett. 104 (2010) 085503.

[81] E. Spreafico, S. Caravati, M. Bernasconi, First-principles study of liquid and amorphous $InGeTe_2$, Phys. Rev. B 83 (2011) 144205.

[82] J. Akola, R. Jones, Structural phase transitions on the nanoscale: The crucial pattern in the phase-change materials $Ge_2Sb_2Te_5$ and GeTe, Phys. Rev. B 76 (23) (2007) 235201.

[83] J. Goldak, C.S. Barrett, D. Innes, W. Youdelis, Structure of α-GeTe, J. Chem. Phys. 44 (9) (1966) 3323.

[84] T. Chattopadhyay, J.X. Boucherle, H.G. vonSchnering, Neutron diffraction study on the structural phase transition in GeTe, J. Phys. C: Solid State Phys. 20 (10) (1987) 1431.

[85] P. Fons, A.V. Kolobov, M. Krbal, J. Tominaga, K.S. Andrikopoulos, S.N. Yannopoulos, G.A. Voyiatzis, T. Uruga, Phase transition in crystalline GeTe: Pitfalls of averaging effects, Phys. Rev. B 82 (2010) 155209.

[86] T. Matsunaga, P. Fons, A.V. Kolobov, J. Tominaga, N. Yamada, The order–disorder transition in GeTe: Views from different length-scales, Appl. Phys. Lett. 99 (2011) 231907.

[87] M. Xu, Z. Lei, J. Yuan, K. Xue, Y. Guo, S. Wang, X. Miao, R. Mazzarello, Structural disorder in the high-temperature cubic phase of GeTe, RSC Adv. 8 (2018) 17435.

[88] D. Dangić, S. Fahy, I. Savić, Molecular dynamics simulation of the ferroelectric phase transition in GeTe: Displacive or order–disorder character, Phys. Rev. B 106 (2022) 134113.

[89] G.E. Ghezzi, J.Y. Raty, S. Maitrejean, A. Roule, E. Elkaim, F. Hippert, Effect of carbon doping on the structure of amorphous GeTe phase change material, Appl. Phys. Lett. 99 (2011) 151906.

[90] S. Gabardi, E. Baldi, E. Bosoni, D. Campi, S. Caravati, G. Sosso, J. Behler, M. Bernasconi, Atomistic simulations of the crystallization and aging of GeTe nanowires, J. Phys. Chem. C 121 (2017) 23827.

[91] S. Gabardi, G.C. Sosso, J. Behler, M. Bernasconi, Priming effects in the crystallization of the phase change compound GeTe from atomistic simulations, Faraday Discuss. 213 (2019) 287–301.

[92] S. Perego, D. Dragoni, S. Gabardi, D. Campi, M. Bernasconi, Structure and crystallization kinetics of as-deposited films of the GeTe phase change compound from atomistic simulations, Phys. Stat. Solidi RRL 17 (2023) 2200433.

[93] G.C. Sosso, M. Salvalaglio, J. Behler, M. Bernasconi, M. Parrinello, Heterogeneous crystallization of the phase change material GeTe via atomistic simulations, J. Phys. Chem. C 119 (2015) 6428–6434.

[94] D. Acharya, O. Abou El Kheir, D. Campi, M. Bernasconi, Crystallization kinetics of nanoconfined GeTe slabs in GeTe/TiTe$_2$-like superlattices for phase change memories, Sci. Rep. 14 (2024) 3224.

[95] S. Wintersteller, O. Yarema, D. Kumaar, F.M. Schenk, O.V. Safonova, P.M. Abdala, V. Wood, M. Yarema, Unravelling the amorphous structure and crystallization mechanism of GeTe phase change memory materials, Nature Commun. 15 (2024) 1011.

[96] S. Raoux, H.-Y. Cheng, M. Caldwell, H. Wong, Crystallization times of Ge–Te phase change materials as a function of composition, Appl. Phys. Lett. 95 (2009) 071910.

[97] R. Berthier, N. Bernier, D. Cooper, C. Sabbione, F. Hippert, P. Noé, In situ observation of the impact of surface oxidation on the crystallization mechanism of GeTe phase-change thin films by scanning transmission electron microscopy, J. Appl. Phys. 122 (2017) 115304.

[98] M. Agati, C. Gay, D. Benoit, A. Claverie, Effects of surface oxidation on the crystallization characteristics of Ge-rich Ge-Sb-Te alloys thin films, Appl. Surf. Sci. 518 (2020) 146227.

[99] M. Avrami, Kinetics of phase change. II Transformation-time relations for random distribution of nuclei, J. Chem. Phys. 8 (1940) 212.

[100] R.J. Allen, D. Frenkel, P.R. ten Wolde, Simulating rare events in equilibrium or nonequilibrium stochastic systems, J. Chem. Phys. 124 (2006) 024102.

[101] G.C. Sosso, J. Chen, S.J. Cox, M. Fitzner, P. Pedevilla, A. Zen, A. Michaelides, Crystal nucleation in liquids: Open questions and future challenges in molecular dynamics simulations, Chem. Rev. 116 (2016) 7078–7116.

[102] D. Turnbull, J.J. Fisher, Rate of nucleation in condensed systems, J. Chem. Phys. 17 (1949) 71–73.

[103] S. Raoux, W. Welnic, D. Ielmini, Phase change materials and their application to nonvolatile memories, Chem. Rev. 110 (2010) 240–267.

[104] D. Lee, K. Lee, D. Yoo, W. Jeong, S. Han, Crystallization of amorphous GeTe simulated by neural network potential addressing medium-range order, Comput. Mater. Sci. 181 (2020) 109725.